THESIS FOR THE DEGREE OF DOCTOR OF PHILOSOPHY

Light–Matter Interaction and Hot Carriers: From Weak to Strong Coupling

JAKUB FOJT

Department of Physics
CHALMERS UNIVERSITY OF TECHNOLOGY
Göteborg, Sweden 2025

Light–Matter Interaction and Hot Carriers: From Weak to Strong Coupling JAKUB FOJT

© Jakub Fojt, 2025

ISBN 978-91-8103-276-5 Doktorsavhandlingar vid Chalmers tekniska högskola. Ny serie nr 5734 ISSN 0346-718X

Department of Physics Chalmers University of Technology SE-412 96 Göteborg, Sweden Telephone +46 (0)31 772 10 00

Cover: Beam of light illuminating a nanoparticle in a cavity producing hot carriers.

Typeset in X₇MT_FX using the Memoir class. Template by M. Petisme and J. M. Rahm.

Chalmers digitaltryck Göteborg, Sweden 2025

Light–Matter Interaction and Hot Carriers: From Weak to Strong Coupling

JAKUB FOJT Department of Physics Chalmers University of Technology

Abstract

When an object is illuminated, it can both scatter and absorb the incoming light. Shortly after absorption, hot carriers, which are electrons and holes with non-thermal energies, form in the material. Scattering, absorption and the formation of hot carriers are fundamental for technologies such as sensing, photovoltaics, and photocatalysis. One way toward better devices is the confinement of light to traditional cavities or metallic nanoparticles. This increases the interaction strength, or coupling, between light and matter. A recent development is the realization of strong coupling – interaction strengths so large that hybrid light–matter states with new properties emerge. In practice, the design space of materials is large, and computational methods can serve as a guide for their rational design, both in the weak and strong coupling regimes.

As part of this thesis, I have developed an analysis software. I use it to show that locally alloying the surface of noble metal nanoparticles with less noble elements is a possible way to control the energies of hot holes. I also show that the probability of generating one hot carrier in the nanoparticle and its opposite carrier in a nearby molecule sensitively and non-monotonically depends on adsorption site and distance, providing valuable insights into the understanding of hot-carrier devices.

In the context of strong coupling, I show that by coupling the nanoparticle to an optical cavity, the absorption spectrum can be tuned to be more optimal for hot–carrier generation. I also derive a computationally efficient and nearly–quantitative model for optical spectra of strongly coupled nanoparticle–molecule assemblies, based on dipolar coupling between moieties. Finally, I implement efficient machine learning models for potential energy surfaces and dipole moments, and apply these to study chemical kinetics under strong coupling conditions.

Keywords: nanoparticles, strong coupling, hot carriers, nanoplasmonics

LIST OF APPENDED PAPERS

This thesis consists of a background to the field and the following papers. It is partly based on the author's licentiate thesis (J. Fojt, *Hot–carrier generation and strong coupling in metal nanoparticles* (2023)).

I Tailoring Hot-Carrier Distributions of Plasmonic Nanostructures through Surface Alloying

Jakub Fojt, Tuomas P. Rossi, Priyank V. Kumar, and Paul Erhart *ACS Nano* **18**, 6398 (2024)

doi: 10.1021/acsnano.3c11418

II Hot-Carrier Transfer across a Nanoparticle-Molecule Junction: The Importance of Orbital Hybridization and Level Alignment

Jakub Fojt, Tuomas P. Rossi, Mikael Kuisma, and Paul Erhart Nano Letters **22**, 8786 (2022)

doi: 10.1021/acs.nanolett.2c02327

III Dipolar Coupling of Nanoparticle–Molecule Assemblies: An Efficient Approach for Studying Strong Coupling

Jakub Fojt, Tuomas P. Rossi, Tomasz J. Antosiewicz, Mikael Kuisma, and Paul Erhart *The Journal of Chemical Physics* **154**, 094109 (2021)

doi: 10.1063/5.0037853

IV Controlling Plasmonic Catalysis via Strong Coupling with Electromagnetic Resonators

Jakub Fojt, Paul Erhart, and Christian Schäfer

Nano Letters 24, 11913 (2024)

doi: 10.1021/acs.nanolett.4c03153

V Machine Learning for Polaritonic Chemistry: Accessing Chemical Kinetics

Christian Schäfer, Jakub Fojt, Eric Lindgren, and Paul Erhart Journal of the American Chemical Society **146**, 5402 (2024)

doi: 10.1021/jacs.3c12829

VI rhodent: A Python package for analyzing real-time TDDFT response

Jakub Fojt, Tuomas P. Rossi, and Paul Erhart *In manuscript*

The author's contribution to the papers:

- I performed the density-functional theory and time-dependent density-functional theory calculations, prepared the figures, and wrote the paper with assistance from my co-authors.
- II I improved the tools used for post-processing and analyzing the time-dependent density-functional theory outputs, performed the density-functional theory and time-dependent density-functional theory calculations, prepared the figures and wrote the paper with assistance from my co-authors.
- III I contributed to the implementation of the dipolar-coupling code, carried out the calculations, prepared the figures, and contributed to the writing of the paper.
- IV I performed the density-functional theory and time-dependent density-functional theory calculations, prepared the figures and wrote the paper with assistance from my co-authors.
- V I wrote the code implementing the cavity and interfaced it with the two machine-learning models (potential energy surface and dipole). I performed the molecular dynamics simulations, prepared part of the figures and contributed to the writing of the paper.
- VI I wrote the software with assistance from my co–authors, including the documentation and tutorials. I ran the density–functional theory and time–dependent density–functional theory calculations for the examples in the paper, prepared the figures and wrote the paper with assistance from my co–authors.

PUBLICATIONS NOT INCLUDED IN THIS THESIS

GPAW: An Open Python Package for Electronic Structure Calculations

Jens J. Mortensen, Ask H. Larsen, Mikael Kuisma, Aleksei V. Ivanov, Alireza Taghizadeh, Andrew Peterson, Anubhab Haldar, Asmus O. Dohn, Christian Schäfer, Elvar Ö. Jónsson, Eric D. Hermes, Fredrik A. Nilsson, Georg Kastlunger, Gianluca Levi, Hannes Jónsson, Hannu Häkkinen, Jakub Fojt, Jiban Kangsabanik, Joachim Sødequist, Jouko Lehtomäki, Julian Heske, Jussi Enkovaara, Kirsten T. Winther, Marcin Dulak, Marko M. Melander, Martin Ovesen, Martti Louhivuori, Michael Walter, Morten Gjerding, Olga Lopez–Acevedo, Paul Erhart, Robert Warmbier, Rolf Würdemann, Sami Kaappa, Simone Latini, Tara M. Boland, Thomas Bligaard, Thorbjørn Skovhus, Toma Susi, Tristan Maxson, Tuomas Rossi, Xi Chen, Yorick L. A. Schmerwitz, Jakob Schiøtz, Thomas Olsen, Karsten W. Jacobsen, and Kristian S. Thygesen

The Journal of Chemical Physics 160, 092503 (2024)

doi: 10.1063/5.0182685

Origin of Macroscopic Observables of Strongly Coupled Metal Nanoparticle–Molecule Systems from Microscopic Electronic Properties

Maria Bancerek, Jakub Fojt, Paul Erhart, and Tomasz J. Antosiewicz *The Journal of Physical Chemistry C* **128**, 9749–9757 (2024)

doi: 10.1021/acs.jpcc.4c02200

List of abbreviations

```
DC dipolar coupling. 30–33, 55, 56
DF dielectric function. 10–12, 14, 42, 43
DFT density–functional theory. 3, 6, 8, 9, 13, 14, 36, 39, 46, 47, 49, 50
DOS density of states. 8, 9, 13, 22
```

EM electromagnetic. 1, 2, 10, 26, 29, 39, 41, 42, 56

FWHM full width at half maximum. 15, 17, 21, 22

GGA generalized-gradient approximation. 48 **GLLB** Gritsenko-van Leeuwen-van Lenthe-Baerends. 48, 49

HC hot carrier. 1–3, 10, 14–20, 23, 33, 35, 49, 55, 56 **HE** hot electron. 17, 18, 21, 22 **HH** hot hole. 17–20 **HOMO** highest occupied molecular orbital. 21

IR infrared. 35, 41

KS Kohn-Sham. 46-48, 50

LCAO linear combination of atomic orbitals. 3, 6, 8 LP lower polariton. 25, 32, 34, 35 LSP localized surface plasmon. 2, 10, 12–16, 18–23, 26, 32–35 LUMO lowest unoccupied molecular orbital. 20–22

NP nanoparticle. 2, 3, 9–14, 16–23, 30, 32–35, 55, 56

PDOS projected density of states. 9, 21, 22 **PES** potential energy surface. 36, 40, 41, 56 **PTA** 1–phenyl–2–trimethylsilylacetylene. 36

RT-TDDFT real-time time-dependent density functional theory. 14–16, 18–20, 33, 36, 50, 52, 55, 56

SC strong coupling. 2, 25, 26, 28–30, 32, 33, 35, 36, 56

TCM transition contribution map. 13, 14, 16, 17, 21, 22 **TDDFT** time-dependent density-functional theory. 10, 12, 13, 30, 32, 33, 39, 49, 50, 52

UP upper polariton. 25, 34 **UV** ultraviolet. 1, 2, 41

XC exchange-correlation. 47-50, 56

Contents

Li	st of a	bbreviations	ix			
1	Intr	oduction	1			
2	Hot	carrier generation in metallic nanoparticles	3			
	2.1	Electronic structure of metals and molecules	3			
		2.1.1 One atom	4			
		2.1.2 Two atoms – hybridization of orbitals	6			
		2.1.3 Many atoms – formation of bands	8			
	2.2	Interaction with light	10			
		2.2.1 Optical properties from the macroscopic perspective	10			
		2.2.2 Optical properties from the quantum perspective	12			
		2.2.3 Hot-carrier generation	14			
	2.3	Controlling hot–carrier generation	18			
		2.3.1 Spatial and energetic control of hot holes	18			
		2.3.2 Increasing the probability of direct transfer	20			
3	Stro	ng coupling	25			
	3.1	3.1 Principles of strong coupling				
		3.1.1 Coupled harmonic oscillators	26			
	3.2	Exploiting strong coupling	29			
		3.2.1 Dipolar coupling	30			
		3.2.2 Increasing hot-carrier generation	33			
		3.2.3 Modifying reaction rates through vibrational strong coupling .	35			
4	Com	nputational methods	39			
	4.1	Fundamental equations	39			
		4.1.1 Interaction of nuclei and electrons with light	41			
	4.2	Continuum matter electrodynamics	42			
		4.2.1 Dipole expansion of the electric field	43			
		4.2.2 The single–photonic mode cavity	45			

Contents

	4.3	Densi	ty functional theory	45
		4.3.1	Kohn–Sham density functional theory	46
		4.3.2	The exchange-correlation functional	48
	4.4	Time-	-dependent density functional theory	49
		4.4.1	Linear response	50
		4.4.2	Efficient response calculation in the linear response regime	52
5	Out	look		55
A	know	ledgme	ents	57
Bi	bliog	raphy		59
Pá	pers l	I-VI		69

1

Introduction

Bright and shiny, colorful, transparent, or opaque – our first impression of any object is shaped by its appearance. Light-matter interaction is responsible for not only our ability to distinguish materials by sight but also many technological applications. Photovoltaic materials convert light into electric energy [1], photocatalysts and photoelectrocatalysts use light to steer chemical reactions or create fuels [2, 3], and optical sensors measure material properties based on their scattering and absorption of light [4]. These technologies are promising for clean [1, 2] and safe [4] energy sources, and a more efficient use of energy in industrial processes [3]. However, generally, only about 20 % of the absorbed light is utilized by commercial solar cells, and roughly 10 % in photocatalytic hydrogen fuel production [5]. Considering the climate crisis [6], the effort to improve materials for these purposes is worthwhile.

The appearance of a material is not everything – what is on the inside matters just as much. Electrons in the material acquire the excess energy when visible or near ultraviolet (UV) light is absorbed. The excited electrons, and the holes they leave behind, are called hot carriers (HCs), owing to their high energies compared to thermal equilibrium. HCs can carry energy out of the material – through the electrodes of a solar cell, or into reactants in the photocatalytic device. One of the main challenges for better devices is to control the energies and spatial localization of HCs, so that they can be extracted before their energy is lost. Theoretical modeling can help us understand these processes. However, practical computations are difficult due to the vastly different time scales of electron dynamics and chemical reactions.

This thesis focuses on light-matter interactions in environments where light – or, more precisely, the modes of the electromagnetic (EM) field – is confined to small volumes. Such confinement enhances the coupling between light and matter, leading to more effective energy exchange between the EM field and the matter degrees of freedom. The canonical example of confined light is a cavity formed by two closely spaced

mirrors, but there are also other realizations. Metallic nanoparticles (NPs) are one such realization. They effectively confine visible and near UV light to the volume of the NP, thanks to a collective mode of electron motion known as the localized surface plasmon (LSP). I recurrently use NPs as a platform for confinement of light, as their properties easily can be tuned through size, shape and composition.

I address two distinct regimes of increased light-matter coupling [7]. These regimes can be used to categorize my work into two themes. In the weak coupling regime (Papers I–II), the increased coupling leads to a higher rate of HC generation or nuclear motion. In the strong coupling (SC) regime (Papers III–V), energy is coherently exchanged between the EM field and the material. Hybrid states of light and matter form, that have energies that differ from the underlying EM mode and electronic or nuclear state(s) [7]. Besides a higher rate of HC generation, the HCs are thus generated at different energies in the SC regime. Additionally, as part of my research, I have written an open–source software (Paper VI) that I have used to model HC generation throughout the thesis.

The aim of this thesis is to shed light on processes of technological importance related to the light-matter interaction – from the weak to the strong coupling regime. I use computational models for the electronic structure in an attempt to answer several questions. How should NPs be designed at the atomic scale to improve HC generation rates? How should they be designed to control energies and spatial localization of HCs? What are the novel improvements enabled by SC in this regard?

Modeling large assemblies and HC-induced chemical reactions remains challenging, as accurate electronic structure methods scale poorly with system size and are intractable at the long time scales of nuclear motion. In this thesis, I also explore approximate methodologies that aim to circumvent these limitations.

The structure of this thesis is such that I first discuss my work in relation to the questions posed above, and then provide a deeper theoretical background supporting this work. I discuss HC generation in metallic nanoparticles in Chapter 2. Then I introduce SC in Chapter 3 and demonstrate its role in modifying absorption spectra, HC generation rates, and chemical reaction rates. In both of these chapters I make references to Chapter 4, where I review the fundamental theory and outline the computational approaches. Finally, I tie together Papers I–VI and provide a perspective on future work in Chapter 5.

Hot carrier generation in metallic nanoparticles

The absorption of light by an object causes electrons in the material to become excited. The energies of these excited electrons and holes exceed those found in equilibrium at room temperature, which has given rise to the term hot carriers (HCs). In this chapter, I give a background on the microscopic mechanisms for HC generation and transfer in metallic nanoparticles (NPs). Then, I show a few examples from Papers I and II of how HC formation can be controlled. A deeper theoretical background for this chapter is provided in Chapter 4.

2.1 Electronic structure of metals and molecules

In order to discuss the connection between atomic structure and HC generation in NPs, a review of basic chemical principles is warranted. Following the book by Sutton [8], I introduce the concept of atomic s, p, and d orbitals, and how they hybridize to form molecular states and metal bands in many—atom systems. Relatively simple models, such as the hydrogen atom and the non self-consistent linear combination of atomic orbitals (LCAO) method, are enough to explain much of the chemistry in this thesis on a qualitative level. At the end of this section, I calculate the electronic structure of Ag NPs using density—functional theory (DFT), the details of which are covered in Chapter 4. These results are sufficiently accurate to, later in the chapter, serve as a foundation for the discussion of HC generation.

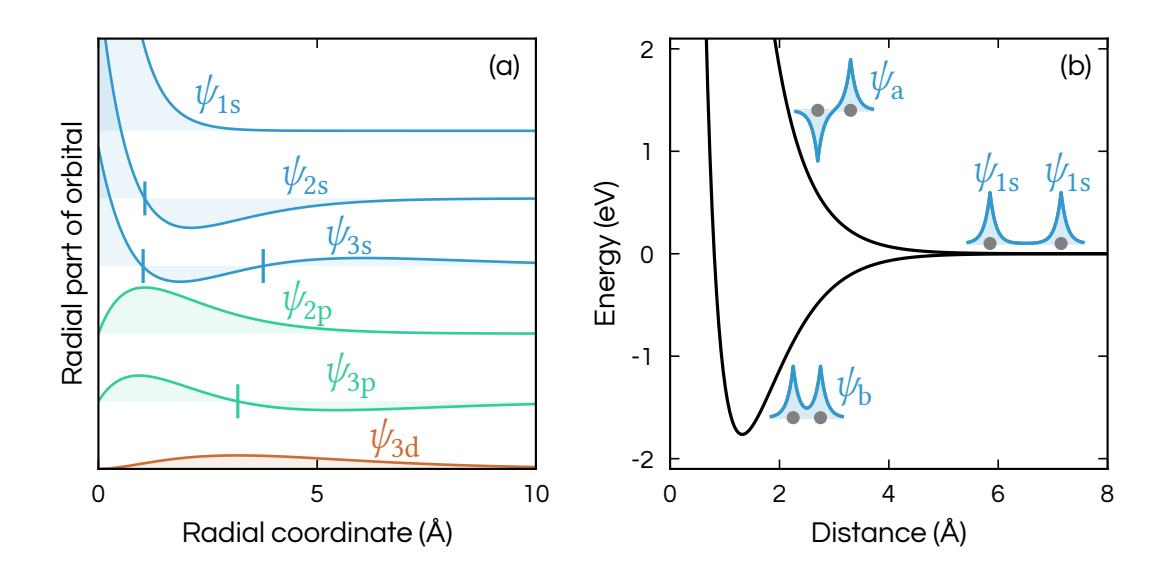


Figure 2.1: (a) Radial part of the first hydrogen orbitals. Nodes (zero crossings) are marked by vertical lines. (b) Hybridization of the 1s orbital in a hydrogen dimer. Energies are shown relative to the energy of two infinitely separated 1s states. At large separation, there are two non-overlapping 1s states centered around each nucleus with the same energy (shown by the inset to the right). As the separation decreases, bonding and antibonding states form with lower and higher energies compared to the 1s state at far separation (shown by the insets on the left). The bonding state has lower energy because the electron density between the nuclei has an attractive interaction with the nuclei charges. At the smallest distances, the energy of the bonding state increases again due to the repulsion between the nuclei.

2.1.1 One atom

Atoms and molecules are made up of electrons bound to atomic nuclei. The nuclei can in many cases be regarded as classical particles that provide an attractive potential for the electrons¹, while the electrons are quantum particles that are found in discrete states.

Let us first consider one electron bound to an atomic nucleus [8, Chapter 1]. The allowed states ψ_n and energies E_n of the electron are the solutions to the Schrödinger equation

$$H\psi_n = E_n \psi_n, \tag{2.1}$$

where H is the Hamiltonian that has the real-space representation (compare to Eq. (4.2))

$$H = -\frac{\hbar^2 \nabla^2}{2m} + V(\mathbf{r}). \tag{2.2}$$

¹This is known as the Born–Oppenheimer [9] or clamped–nuclei approximation and works well for the situations considered in this thesis [10, Chapter 3].

The first term of the Hamiltonian is related to the kinetic energy of the electron and the second term is the potential it feels from the nucleus. \hbar is the reduced Planck constant and m the electron mass. At rest, the electron occupies the state with the lowest energy, called the ground state, but interactions with light can excite the electron to higher-lying states. The states are represented in real space by the wave function $\psi_n(r)$, with $|\psi_n(r)|^2$ being the electron density. The wave functions of such a single atom system are also called orbitals. States are orthonormal so that the integral over all space $\int \psi_n^*(r) \psi_m(r) dr$ is 1 if m and n are the same state, and 0 otherwise.

For a spherically symmetric potential V(r) = V(r), the wave functions take the separable form $\psi(r) = R(r)Y(\theta,\phi)$, where R(r) is a radial function and $Y(\theta,\phi)$ are spherical harmonics. The exact forms of the latter can be found, e.g., in Sutton [8, Chapter 1] or Ref. [10, Appendix K]. For this discussion it is sufficient to say that the first spherical harmonic is uniform $Y(\theta,\phi)=1$, and all others are ordered by increasing complexity. For historical reasons, the first spherical harmonics in order are denoted by the letters s, p and d. There are 3 harmonics of p symmetry which are identical except for a rotation, and there are 5 harmonics of d symmetry. The set of orbitals with the same spherical harmonic and the same number of nodes is called a shell.

For the hydrogen atom, where V(r) is exactly the Coulomb potential of a point charge (see Eq. (4.2)), there are closed–form solutions for the orbitals, which can be found in, e.g., Ref. [11, Chapter 4]. These solutions are plotted in Fig. 2.1a. However, the following properties will hold in general.² The lowest energy state must have the least varying curvature, in order to minimize the second derivative ∇^2 of the kinetic energy. This will be satisfied by a smoothly decreasing radial part and the s spherical harmonic, called the 1s orbital. The next s orbitals (called 2s, 3s, ...) must have increasing numbers of nodes (zero crossings) in order to satisfy the orthogonality condition. Each node forces a change in curvature and thus results in a higher energy. Orbitals with different spherical harmonics are orthogonal even if they have the same radial part, so the first p and d orbitals have zero node crossings. The conventional numbering of the p orbitals starts from 2 and of d orbitals from 3. The precise form of the potential determines the relative energies of orbitals with different spherical harmonics, but often the order of the first orbitals is [8, Chapter 1]

$$1s < 2s < 2p < 3s < 3p < 3d$$
.

Of course, most atoms contain more than one electron. This renders the electronic structure problem much more difficult. A common approach is to construct the electronic state from a set of single-electron orbitals. According to the so-called *aufbau* principle, these orbitals are filled sequentially in order of increasing energy, with each orbital accommodating at most two electrons (due to the two spin degrees of freedom). Then the s, p, and d shells can be occupied by at most, 2, 6 and 10 electrons respectively. In order for such a scheme to quantitatively give the right results, the potential

²At least if the magnitude of the potential is smoothly decreasing.

in Eq. (2.2) needs to incorporate effects of electron–electron interaction. In fact, this treatment can be made formally exact, like in DFT which I discuss in Chapter 4, but nevertheless in practice always involves some approximations. It is also a general property of atoms, that when one shell is completely occupied by electrons, then its energy is considerably lowered by the electron–electron interactions. Thanks to this property, most electrons are bound so tightly to the nucleus that they do not form chemical bonds with other atoms. Those are called core electrons, while the remainder are valence electrons. For example, in Ag, core electrons occupy shells up to 4s, 4p, and 3d, and there are 10 valence electrons in the 4d orbitals and 1 valence electron in the 5s orbital.

2.1.2 Two atoms – hybridization of orbitals

Now, we consider one electron around two atoms [8, Chapter 2]. This could, for example, be the case of the ionized ${\rm H_2}^+$ molecule, but I will keep the calculations general. The Hamiltonian for this system is (again, compare to Eq. (4.2))

$$H = -\frac{\hbar^2 \nabla^2}{2m} + V_1(|\mathbf{r} - \mathbf{R}_1|) + V_2(|\mathbf{r} - \mathbf{R}_2|) + \frac{e^2}{4\pi\varepsilon_0} \frac{Z_1 Z_2}{|\mathbf{R}_1 - \mathbf{R}_2|},$$
 (2.3)

where I have assumed that there are two spherical potentials around the positions of the nuclei R_1 and R_2 . The final term is the Coulomb repulsion between the nuclei where Z_1 and Z_2 are the atomic numbers of the nuclei, ε_0 the vacuum permittivity, and e the elementary charge. An approximate solution for the system can be obtained using the LCAO method, where the states of this system are required to be linear combinations

$$\psi = c_1 \psi_1 + c_2 \psi_2 \tag{2.4}$$

of one basis state each ψ_1 and ψ_2 . I will use the LCAO method in a non self-consistent fashion where ψ_1 and ψ_2 are simply taken to be solutions to a Hamiltonian of the form Eq. (2.2) for atoms 1 and 2. The two basis states are not orthogonal but have a finite overlap $S_{12} = \langle \psi_2 | \psi_1 \rangle^3$. Since there are two basis states, there will be two solutions. They can be found easily in the special case that atoms 1 and 2 are identical. Then, swapping the indices 1 and 2 may not result in a change in electron density $|\psi(r)|^2$, and the only two solutions are $c_1 = c_2$ and $c_1 = -c_2$. Requiring the states to be normalized gives the two solutions

$$\psi_b = \frac{1}{\sqrt{2(1+S_{12})}} (\psi_1 + \psi_2) \tag{2.5}$$

$$\psi_a = \frac{1}{\sqrt{2(1 - S_{12})}} (\psi_1 - \psi_2), \qquad (2.6)$$

³Here, I have used the bra-ket notation where $\langle \psi_2 | \psi_1 \rangle = \int \psi_2^*(\mathbf{r}) \psi_1(\mathbf{r}) d\mathbf{r}$ is the overlap integral of two states and $\langle \psi_2 | O | \psi_1 \rangle = \int \psi_2^*(\mathbf{r}) O \psi_1(\mathbf{r}) d\mathbf{r}$ denotes the integral with respect to an operator O.

corresponding to a bonding and anti-bonding state, respectively. In the bonding state, there is electron density between the nuclei which lowers the electrostatic energy and has a cohesive effect on the molecule, while the opposite is true for the anti-bonding state (Fig. 2.1b; insets).

The energies of the two states can be found by projecting the Schrödinger equation on the basis state for one of the atoms

$$\langle \psi_1 | H | \psi_b \rangle = E_b | \psi_b \rangle \tag{2.7}$$

$$\langle \psi_1 | H | \psi_a \rangle = E_a | \psi_a \rangle, \tag{2.8}$$

which gives, after plugging in the solutions and rearranging,

$$E_b = \frac{H_{11} + H_{12}}{1 + S_{12}} \tag{2.9}$$

$$E_a = \frac{H_{11} - H_{12}}{1 - S_{12}}. (2.10)$$

Here, I have introduced the matrix elements of the Hamiltonian $H_{ij} = \langle \psi_j | H | \psi_i \rangle$ for i and j = 1, 2, which can be computed numerically for any given basis states. For this purpose, it is convenient to use that the Hamiltonian Eq. (2.3) is the Hamiltonian of atom 1, plus the potential from atom 2 and the Coulomb repulsion E_{nuclei} of the nuclei, where

$$E_{\text{nuclei}} = \frac{e^2}{4\pi\varepsilon_0} \frac{Z_1 Z_2}{|R_1 - R_2|}.$$
 (2.11)

Then the relation $\langle \psi_1 | H = \langle \psi_1 | (E_0 + E_{\text{nuclei}}) + \langle \psi_1 | V_2 \text{ holds, where } E_0 \text{ is the energy of the basis states. This gives the energies}$

$$E_b = E_0 + E_{\text{nuclei}} + \frac{\langle \psi_1 | V_2 | \psi_1 \rangle + \langle \psi_1 | V_2 | \psi_2 \rangle}{1 + S_{12}}$$
 (2.12)

$$E_a = E_0 + E_{\text{nuclei}} + \frac{\langle \psi_1 | V_2 | \psi_1 \rangle - \langle \psi_1 | V_2 | \psi_2 \rangle}{1 - S_{12}}.$$
 (2.13)

The three overlap integrals S_{12} , $\langle \psi_1 | V_2 | \psi_1 \rangle$ and $\langle \psi_1 | V_2 | \psi_2 \rangle$ can be numerically computed, which I have done for the hydrogen is orbitals. I have plotted the energies $E_b - E_0$ and $E_a - E_0$ in Fig. 2.1b as functions of distance. At far distances, there is little overlap between the hydrogenic orbitals, and the electrostatic attraction of the orbital to the opposite nucleus $\langle \psi_1 | V_2 | \psi_1 \rangle$ is the dominating term, which is almost exactly cancelled by E_n . When the orbitals start to overlap significantly around 4 Å, the energies of the two states start to split, and the magnitude of this split increases with decreasing distance.

As in the one-atom system, the *aufbau* principle is used here to construct many-electron systems. For a two-electron system, both electrons would occupy the bonding state $|\psi_b\rangle$.

2.1.3 Many atoms – formation of bands

The LCAO method can be used for any number of nuclei, with any number of basis states, in schemes of variable complexity. The procedure involves calculating overlap integrals numerically and solving linear systems of equations. For the purpose of this thesis, I will state one more result from the non self-consistent LCAO method, before I show accurate calculations done using DFT. If one considers N identical nuclei with one basis state each, assumes the overlap integrals $\langle \psi_j | \psi_i \rangle$ to be zero (this cannot hold exactly, but simplifies the calculations), the on–site Hamiltonian matrix elements $\langle \psi_i | H | \psi_i \rangle = \alpha$ and next–neighbor elements $\langle \psi_j | H | \psi_i \rangle = \beta$, then the energies of the N states are [8, Chapter 3]

$$E_n = \alpha + 2\beta \cos\left(\frac{n\pi}{N+1}\right), \quad \text{for } n = 1, \dots, N.$$
 (2.14)

This shows that for systems with an increasing number of interacting atoms, the spacing between energies of subsequent states decreases. As the number of atoms tends to infinity, a continuum of states called a band forms between $E = \alpha - 2\beta$ and $\alpha + 2\beta$. The width of the band is controlled by the overlap between neighbors β , while the on–site overlap α determines its center.

The non self-consistent LCAO energies Eq. (2.14) can be compared to the energies ε_n of a DFT calculation (Eq. (4.37)) for bulk Ag. I have made a series of such calculations with various values of the lattice spacing. Fig. 2.2a shows the density of states (DOS), which is simply a broadening of discrete energies onto a continuous grid, DOS(ε) = $\sum_n G(\varepsilon - \varepsilon_n)$. For this plot, Gaussians $G(\varepsilon)$ are defined

$$G(\varepsilon) = (2\pi\sigma^2)^{-1/2} \exp\left[-\varepsilon^2/2\sigma^2\right],$$
 (2.15)

where $\sigma=0.05\,\mathrm{eV}$. The energies in the plot are given with respect to the Fermi level, which, in a metal, is the energy of the last occupied electron. Then states at negative energies are fully occupied, states at positive energies fully unoccupied and states at the Fermi level partially occupied. As the Ag structure is made artificially sparse (lattice constant of 12.2 Å, about three times the equilibrium value), there are only valence orbitals 4d, 5s, and 5p, like in an isolated Ag atom. The 4d orbital is occupied by 10 electrons per atom and the 5s orbital is occupied by one electron per atom. Shrinking the structure, the 5s and 5p orbitals are the first to hybridize. A qualitative comparison to Eq. (2.14) can be made by imagining that the longer extent of those functions effectively gives a finite β already at 8 Å. At the equilibrium lattice constant (4.1 Å), the 5s and 5p states have hybridized into a wide sp-band that has equal proportions of s and p character everywhere. The 4d orbital has hybridized into a much more narrow d-band, due to the shorter extent of the atomic orbitals.

The narrow energetic extent of the d-band is directly related to a strong degree of localization in real space. While the sp-states are delocalized over the entire metal, the

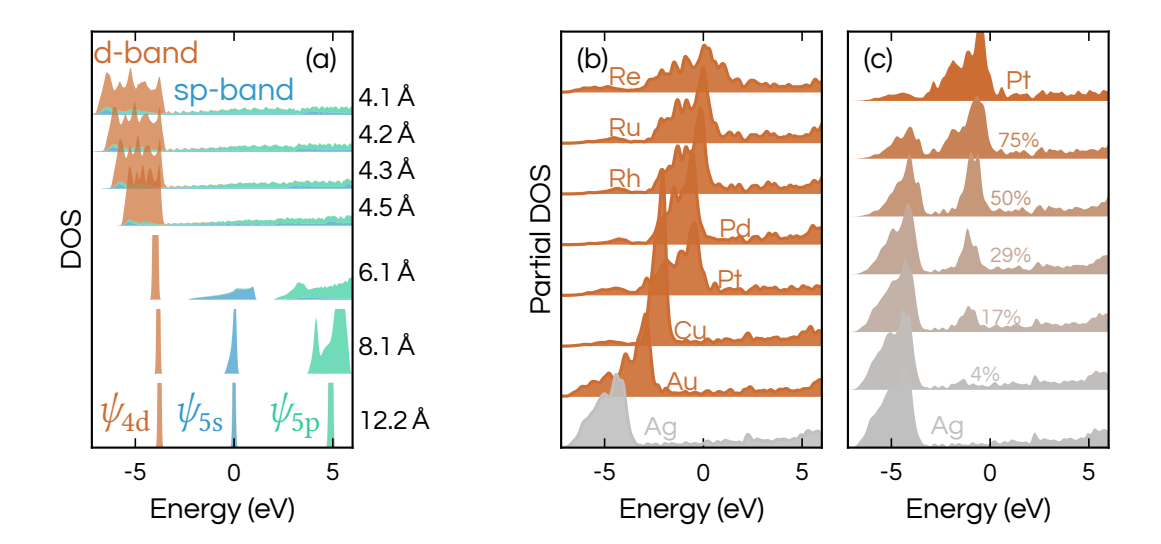


Figure 2.2: DOS and projected density of states (PDOS) from DFT calculations. Energies are given with respect to the Fermi level, so that states at negative energies are occupied and positive unoccupied. (a) DOS of bulk Ag, for different values of the lattice spacing. Colors indicate s, p and d character of the DOS. (b–c) PDOS in the surface layer of a Ag NP, as (b) the surface alloyant is varied at a fixed 100 % surface concentration, and (c) the surface alloy concentration is varied for a Pt alloyant. Colors indicate alloy concentration and species.

d states are localized to regions close to the atomic nuclei. This is illustrated in **Paper I**, where series of Ag NPs with alloyed surfaces were constructed. These NPs consist of 269 atoms, and measure 1.2 nm-by-2.0 nm. The PDOS in the surface is obtained from DFT calculations, and shown in Fig. 2.2b-c. This PDOS is defined similarly to the DOS, PDOS(ε) = $\sum_n w_n G(\varepsilon - \varepsilon_n)$, with the additional weight w_n between 0 and 1 that measures whether the state is localized to the surface. From these plots, it is clear that shape of the d-band in the surface PDOS is determined by the species in the surface, and not in the bulk (which is always Ag).

In the series of 100 %-alloyed surfaces with different alloy species (Fig. 2.2b), it is clear how the d-band changes between the alloy species, while the sp-band remains almost unchanged. Out of the considered metals, the group 11 elements Ag, Au and Cu have the deepest d-bands (respectively 3.8, 2.5, and 1.8 eV below the Fermi level). These elements have one electron per atom in an s state, which needs to fit below the Fermi level. This pushes the d-band deep below the Fermi level. Pt and Pd are group 10 elements with one electron fewer than the group 11 elements. Their d-bands end right at the Fermi level. Rh, Ru and Re follow in groups 9-7 with partially unoccupied d-bands.

A series of NPs with varied Pt surface alloy concentration from 0 to 100 % was also considered in Paper I. The PDOS for this series (Fig. 2.2c) shows a mix of the Ag and Pt d-bands. Notably, at low concentrations, the Pt-peak of the d-band is relatively narrow,

as most neighbors are Ag atoms, and hybridize to a lesser extent due to the energetic misalignment. Later in this chapter, I show how the energetic and spatial localization of the d states can be used to control HC distributions.

2.2 Interaction with light

In a metal, electrons in the sp-band are often called free electrons, because they can easily be displaced by external electric fields [8, Chapter 7]. Free electrons are able to move collectively in metal, and in a constrained geometry such as a NP, this mode of motion can be excited by light [12]. The mode is known as the localized surface plasmon (LSP). The LSP typically decays into HCs within less than 100 fs [13], or even few tens of fs in a small NP [14–16].

A simple explanation of the LSP is provided through macroscopic theory, where the electrons are treated as a continuum charge density within the material. In Sect. 2.2.1, I use this macroscopic theory to calculate absorption spectra, showing that the absorption cross section becomes very large at frequencies resonant with the LSP. However, to describe the subsequent generation of HCs, it is necessary to account for the electronic structure explicitly. To this end, I perform time—dependent density—functional theory (TDDFT) calculations for a Ag NP, first obtaining absorption spectra in Sect. 2.2.2, and then analyzing HC generation in Sect. 2.2.3.

2.2.1 Optical properties from the macroscopic perspective

Let us forget about the quantum states of electrons for a moment, and regard matter as a continuum characterized by a frequency-dependent dielectric function (DF) $\varepsilon(\omega)$. Here, I follow Ref. [12], to show how the LSP appears in this picture. The fundamental equation is Gauss's law Eq. (4.16), which requires that

$$\varepsilon(\omega)\nabla \cdot \mathbf{E}(\omega) = 0. \tag{2.16}$$

In bulk materials, i.e., where the DF is spatially uniform everywhere, Eq. (2.16) can always be satisfied by Fourier components of the electric field $E(\omega)$ that are purely transversal ($\nabla \cdot E(\omega) = 0$). This corresponds to a propagating wave, just like electromagnetic (EM) radiation in vacuum. However, if $\varepsilon(\omega) = 0$ for some frequency, then also a longitudinal mode $\nabla \cdot E(\omega) \neq 0$ is allowed. This mode corresponds to the polarization of free charge in the material, i.e., a collective movement of electrons, and is called a bulk plasmon. This condition can only be fulfilled by materials that have (almost) free electrons. A simple model that describes such materials is the Drude free–electron model, where the DF is given by

$$\varepsilon(\omega) = 1 - \frac{\omega_p^2}{\omega^2 + i\gamma\omega}.$$
 (2.17)

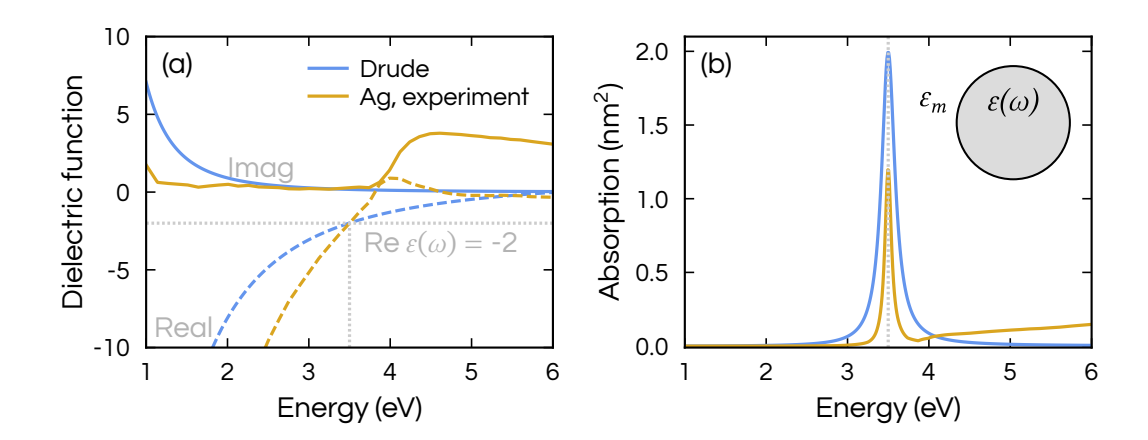


Figure 2.3: (a) DFs for the Drude model and experimentally measured for Ag [17]. (b) Absorption cross sections for the two DFs in panel (a), calculated in the long-wavelength limit of Mie theory. The drawing illustrates that Mie theory gives a solution for the electric field for a sphere with DF $\varepsilon(\omega)$ in an environment ε_m .

The model DF has two parameters: the plasma frequency ω_p and damping constant γ . At the frequency $\omega = \sqrt{\omega_p^2 - \gamma^2} \approx \omega_p$ the real part of $\varepsilon(\omega)$ is zero, allowing a bulk plasmon mode. However, as the imaginary part of $\varepsilon(\omega)$ is finite, the mode is damped and cannot sustain forever without an external driving force.

In the continuum matter picture, a NP can be modeled by considering a DF that has the frequency dependence of our material of interest inside a sphere, and is constant outside it, corresponding to vacuum (sketched in Fig. 2.3b). The solution to Eq. (2.16) for this geometry is given by Mie theory [18]. This yields an expression where the field is an infinite series of spherical harmonics, that can be numerically computed to arbitrary order [19]. The dipolar part gives the polarizability [20]

$$\alpha(\omega) = 4\pi\varepsilon_0 r^3 \frac{\varepsilon(\omega) - 1}{\varepsilon(\omega) + 2},\tag{2.18}$$

where r is the radius of the sphere, c the speed of light, and ε_0 the vacuum permittivity. The imaginary part of the polarizability is related to the absorption cross section through Eq. (4.28). For the Mie sphere, a resonance should appear for frequencies satisfying

Re
$$\varepsilon(\omega) = -2$$
, (2.19)

assuming that the numerator $\varepsilon(\omega)-1$ varies slowly for those frequencies. This condition is satisfied for $\omega=\sqrt{\omega_p^2/3-\gamma^2}\approx\omega_p/\sqrt{3}$ in the Drude model. Fig. 2.3 shows the Drude DF and the corresponding absorption, for a choice of parameters $\omega_p=\sqrt{3}\cdot 3.5$ eV, $\hbar\gamma=0.00$

 $0.2 \, \text{eV}$, and $r = 0.8 \, \text{nm}$. Indeed, the resonance condition is satisfied at $3.5 \, \text{eV}$, which is the LSP resonance, and the absorption spectrum is sharply peaked around this value.

A more realistic NP spectrum is obtained by replacing the Drude DF with an experimentally measured DF for Ag [17] (Fig. 2.3). Due to the presence of bound d -electrons and the possibility of electron emission, the imaginary part of the experimental Ag DF is large at high frequencies. This leads to significant absorption at those frequencies, unlike in the Drude model. Compared to other metals, Ag actually has the sharpest LSP resonance, due to having the lowest imaginary part of the DF at the resonance condition [17, 21]. It is worth noting, that there are also solutions for similar geometries, such as ellipsoids, that give other resonance conditions [22, Chapter 4]. An elongated particle gives a redshifted resonance for polarization along the long axis [20].

2.2.2 Optical properties from the quantum perspective

The absorption spectrum can also be calculated by considering the electrons as quantum particles responding to a perturbation. If the electronic system is much smaller than the wavelengths of interest (which are at least hundreds of nm), the perturbation can be taken to be an electric field E(t) spatially constant over the entire system. In TDDFT, which is described in detail in Sect. 4.4, the single-particle density matrix in the basis of ground state orbitals $\delta \rho_{ia}(t) = \rho_{ia}(t) - \rho_{ia}(0)$, defined in Eq. (4.58), describes the excitations in the system. The matrix element $\delta \rho_{ia}$ is related to the probability of an excitation from an occupied state i (where a hole can form) to an unoccupied state a (to which an electron can be excited)⁴. For sufficiently weak perturbations, the system response is linear and described by the differential equation (repeated in Eq. (4.62))

$$i\hbar \frac{\partial \delta \rho_{ia}(t)}{\partial t} = \hbar \omega_{ia} \delta \rho_{ia}(t) + f_{ia} \mu_{ia} \cdot E(t) + f_{ia} \sum_{ib} K_{ia,jb} \delta \rho_{ia}(t). \tag{2.20}$$

Here, f_{ia} is the occupation number difference between states i and a (which is at most 2) and $\hbar\omega_{ia}$ the difference between the corresponding single-particle energies. The transition dipole moment μ_{ia} describes the coupling strength of each excitation $i \to a$ to the external perturbation. The coupling matrix $K_{ia,jb}$ couples pairs of excitations $i \to a$ and $j \to b$.

Two different TDDFT methods are detailed in Sect. 4.4. In the method known as Casida [23] or linear response TDDFT, one takes the Fourier transform (which I define in Eq. (4.18)) of Eq. (2.20) and solves the linear system of equations Eq. (4.63) for $\delta \rho_{ia}(\omega)$. It is easy to see that if the interactions between excitations are neglected ($K_{ia.ib}=0$),

 $^{^4}$ In the following, it is enough to consider states i that have a larger occupation than states a (see the discussion in Sect. 4.4.1).

then the solution is

$$\delta \rho_{ia}(\omega) = \frac{f_{ia}}{\hbar \omega - \hbar \omega_{ia}} \mu_{ia} \cdot E(\omega). \tag{2.21}$$

Equation (2.21) describes each transition in the non–interacting system as a harmonic oscillator, which couples to the external perturbation through $f_{ia}\mu_{ia}$.

The transition dipole moment can be calculated from a DFT calculation. As an example, I perform such a calculation for the Ag NP used in Paper II. This NP is isotropic, and has an effective radius of about 0.8 nm. The z-component μ_{ia}^z of μ_{ia} is visualized as a transition contribution map (TCM) in Fig. 2.4a. The TCM is a tool for visualization [24] where the quantity of interest, is mapped onto an occupied and an unoccupied energy grid ($\varepsilon_{\rm occ}$ and $\varepsilon_{\rm unocc}$) by a convolution with Gaussians

$$TCM(\varepsilon_{occ}, \varepsilon_{unocc}) = \sum_{ia} f_{ia} \mu_{ia}^z G(\varepsilon_i - \varepsilon_{occ}) G(\varepsilon_a - \varepsilon_{unocc})$$
 (2.22)

The same $\sigma=0.05\,\mathrm{eV}$ is used for the Gaussians as previously, and the DOS is plotted together with the TCM. There are two groups of transitions that are significantly susceptible to the electric field – low energy transitions within the sp–band, and high–energy transitions from the d–band (to the sp–band, making them interband transitions). Most of the low–energy transitions fall in the interval $0.8\,\mathrm{eV} < \hbar\omega_{ia} < 1.8\,\mathrm{eV}$, which is marked by diagonal lines in Fig. 2.4. The transitions from the d–band $\varepsilon_i < -3.8\,\mathrm{eV}$ are to the left of the vertical line in the plot.

The absorption spectrum can be computed from Eq. (4.65) and Eq. (4.26). The polarizability for the non-interacting system is then

$$\alpha(\omega) = -2\sum_{ia} f_{ia} |\boldsymbol{\mu}_{ia}|^2 \left[\frac{\hbar \omega_{ia}}{(\hbar \omega)^2 - (\hbar \omega)_{ia}^2} \right], \tag{2.23}$$

which is a sum of Lorentzians with weights $f_{ia}|\mu_{ia}|^2$. As there is no intrinsic damping to the harmonic oscillators in TDDFT within the adiabatic approximation, the excitations are infinitely sharp. It is customary to introduce an artificial damping through the substitution $\omega \to \omega + i\eta$, in order to plot the spectrum. Using $\eta = 0.05$ eV, the absorption spectrum is plotted in Fig. 2.4b. The non–interacting absorption spectrum has the most weight at those transitions that have the largest transition dipole moments, which gives an absorption maximum around 1.2 eV, much lower than the LSP predicted from Mie theory.

By properly including the coupling between excitations $K_{ia,jb}$, the resonance frequencies of the harmonic-oscillator type excitations are modified⁵. However, the spectrum is still made up of a sum of Lorentzians. I calculate the fully interacting absorption

⁵An example of this phenomenon, which applies also here, is given in Sect. 3.1.1

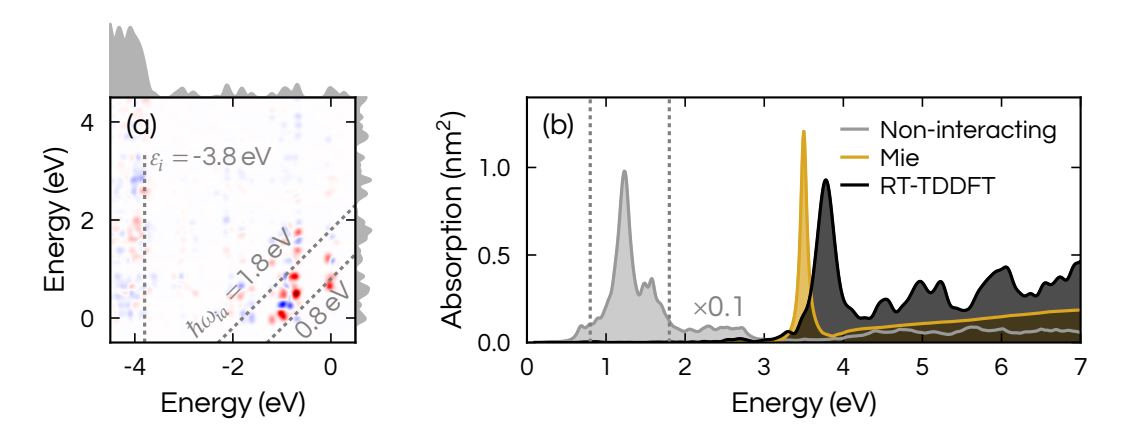


Figure 2.4: (a) Visualization of the transition dipole moment for the Ag NP in the form of a TCM (Eq. (2.22)). The largest transition dipole moments are found between the diagonal lines (0.8 eV $< \hbar \omega_{ia} < 1.8$ eV) and to the left of $\varepsilon_i < -3.8$ eV. (b) Absorption spectrum computed with non-interacting DFT and real-time time-dependent density functional theory (RT-TDDFT). The former has been scaled down by a factor of 0.1. For reference, the Mie spectrum from Fig. 2.3b is also included. The dashed lines in panels (a) and (b) mark the transitions within the range 0.8 eV $< \hbar \omega_{ia} < 1.8$ eV.

spectrum using the RT-TDDFT method, where the equations of state are propagated forward in time. For the Ag NP with a few hundred atoms, with 11 valence electrons per atom, this is computationally cheaper than the Casida method, and for sufficiently weak perturbations yields the same results [25]. The interacting spectrum (Fig. 2.4b) succeeds in capturing the LSP, giving a resonance of 3.8 eV. It should be pointed out that it is a coincidence for this particular NP that the resonance is equal to the d-band onset, other sizes and shapes of Ag NPs can have different resonances. The LSP is slightly blueshifted compared to the Mie result with the experimentally measured DF, which is to be expected given the lack of a non-local description of the DF in Mie theory. Because the part of the material near the surface experiences a different chemical environment than the bulk, the DF should be modified near the edges, resulting in a blue-shift compared to the Mie prediction [26].

2.2.3 Hot-carrier generation

The RT-TDDFT method also gives direct access to time-resolved HC distributions, by simulating the response of $\delta \rho_{ia}(t)$ to a Gaussian laser pulse

$$E(t) = E_0 \cos(\omega_0(t - t_0)) \exp(-(t - t_0)^2 / 2\tau^2). \tag{2.24}$$

The Fourier transform of a Gaussian pulse in the time domain is also a Gaussian in the frequency domain

$$E(\omega) = E_0 \sqrt{2\tau^2/\pi} \exp(i\omega t_0) \exp\left(-(\omega - \omega_0)^2 \tau^2/2\right), \tag{2.25}$$

and the parameters are chosen so that the envelope is centered at $t_0=7\,\mathrm{fs}$, the full width at half maximum (FWHM) in the time-domain is $2\sqrt{2\ln 2}\tau=5.2\,\mathrm{fs}$, and the frequency $\hbar\omega_0=3.8\,\mathrm{eV}$ is resonant with the LSP. Then, the FWHM in the frequency domain $2\sqrt{2\ln 2}\hbar/\tau=0.7\,\mathrm{eV}$ is comparable to the width of the LSP resonance. The transition probability (repeated in Eq. (4.66))

$$P_{ia}(t) = \frac{\left|\delta\rho_{ia}(t)\right|^2}{f_{ia}}.$$
(2.26)

is used to calculate the probability of an electron in state a, or a hole in state i as

$$P_a^{\text{electron}} = \sum_i P_{ia} \tag{2.27}$$

$$P_i^{\text{hole}} = -\sum_a P_{ia},\tag{2.28}$$

where the summations are limited to states i < a. Because the response of the system is linear for weak perturbations, the induced dipole moment is proportional to the field strength $|E_0|$, and the number of HCs to the irradiance $|E_0|^2 \varepsilon_0 c/2$. Therefore, I choose a suitable E_0 for the RT-TDDFT calculations, and refrain from showing absolute magnitudes of the computed quantities in the following plots.

Before computing the response to the pulse using RT-TDDFT, it is instructive to figure out the non-interacting response. If $K_{ia,jb}=0$, then Eq. (2.20) is a first-order inhomogeneous differential equation in time, for each matrix element separately. The solution is

$$\delta \rho_{ia}(t) = \frac{1}{i\hbar} e^{-i\omega_{ia}t} f_{ia} \boldsymbol{\mu}_{ia} \cdot \int_{-\infty}^{t} E(\tau) e^{i\omega_{ia}\tau} d\tau. \tag{2.29}$$

During the duration of the pulse, each matrix element increases in magnitude. However, after the decay of the pulse, the limit in the integral can be taken to infinity, making it exactly the Fourier transform of the perturbation, evaluated at the frequency of the transition $E(\omega_{ia})$. Then, the transition probability of the non-interacting system after the pulse decay is

$$P_{ia} = \frac{f_{ia}}{\hbar^2} \left| \boldsymbol{\mu}_{ia} \cdot \boldsymbol{E}(\omega_{ia}) \right|^2. \tag{2.30}$$

Only excitations resonant with the pulse remain. Each excitation contributes to a sinusoidally oscillating dipole at the frequency ω_{ia} , so the total dipole oscillates indefinitely close to the center frequency of the pulse.

Having computed the interacting response with RT–TDDFT, the induced dipole moment in the Ag NP is plotted in Fig. 2.5a together with the pulse E(t). Like in the non–interacting case, the dipole moment increases during the duration of the pulse, but instead of oscillating indefinitely, it decays over the next 20 fs. The peak in the amplitude of the oscillating dipole moment occurs 1.6 fs after the maximum of the pulse, this is indicated by a vertical line in Fig. 2.5a and the label *peak dipole*. Similarly, the final time of the 30 fs long simulation, is marked by the label *HCs*. The TCM for the transition probability

$$\sum_{ia} P_{ia} G(\varepsilon_i - \varepsilon_{\text{occ}}) G(\varepsilon_a - \varepsilon_{\text{unocc}})$$
 (2.31)

is plotted in Fig. 2.5b–c for those two times. During the time of the peak dipole moment (Fig. 2.5b), most transitions present are the ones with the largest transition dipole moments (compare to Fig. 2.4a), as they are directly excited by the pulse. The low–energy transitions (0.8 eV $< \hbar \omega_{ia} < 1.8$ eV) make up the LSP in this system, and the interband transitions ($\varepsilon_i < -3.8$ eV) the associated screening from the d–band [27]. The collective resonance of these transitions is 3.8 eV, despite the energy differences being around 1 eV (for the low–energy transitions) and above 3.8 eV (for the d–electron screening). This is possible through the large values of the coupling matrix $K_{ia,jb}$ for pairs of such transitions, and physically means that the transitions are strongly coupled to each other.

The excitations making up the screened plasmon are coupled to other excitations in the system through the $K_{ia,jb}$ matrix. Over the duration of the simulation, they decay into HCs in a process known as Landau damping. At the end of the simulation (Fig. 2.5c) the HCs are resonant to the pulse, distributed within the width of the pulse to the line $\hbar\omega_{ia}=\hbar\omega_{0}$, where ω_{0} is the center frequency of the pulse. The distinction between excitations resonant and not–resonant with the pulse can be made more clear by the following weighted distribution of transitions

$$\sum_{ia} P_{ia} G(\hbar \omega_{ia} - \hbar \omega), \tag{2.32}$$

which is plotted as a function of $\hbar\omega$ in Fig. 2.5d. The HCs at the end of the simulation are indeed resonant with the pulse, and symmetrically distributed around the center frequency of the pulse, while the plasmon consists of excitations at many different $\hbar\omega_{ia}$.

The observation that the HCs at the end of the simulation are resonant with the pulse, is related to the HCs being weakly coupled to other excitations through $K_{ia,jb}$, and thus being the most susceptible to oscillation at ω_{ia} (as opposed to the LSP that has a different resonance from the underlying ω_{ia} 's). The distinction between strong and weak coupling will become more clear when I return to this topic in Chapter 3. The linear response of the system is why it is shape of the pulse $|E(\omega)|$ in the frequency domain that determines the frequencies of final transitions – no new frequencies are introduced to the system (in the adiabatic approximation). Effectively, the HCs at the end of the simulation should obey a similar formula to Eq. (2.30), where instead of through μ_{ia} , the transitions couple

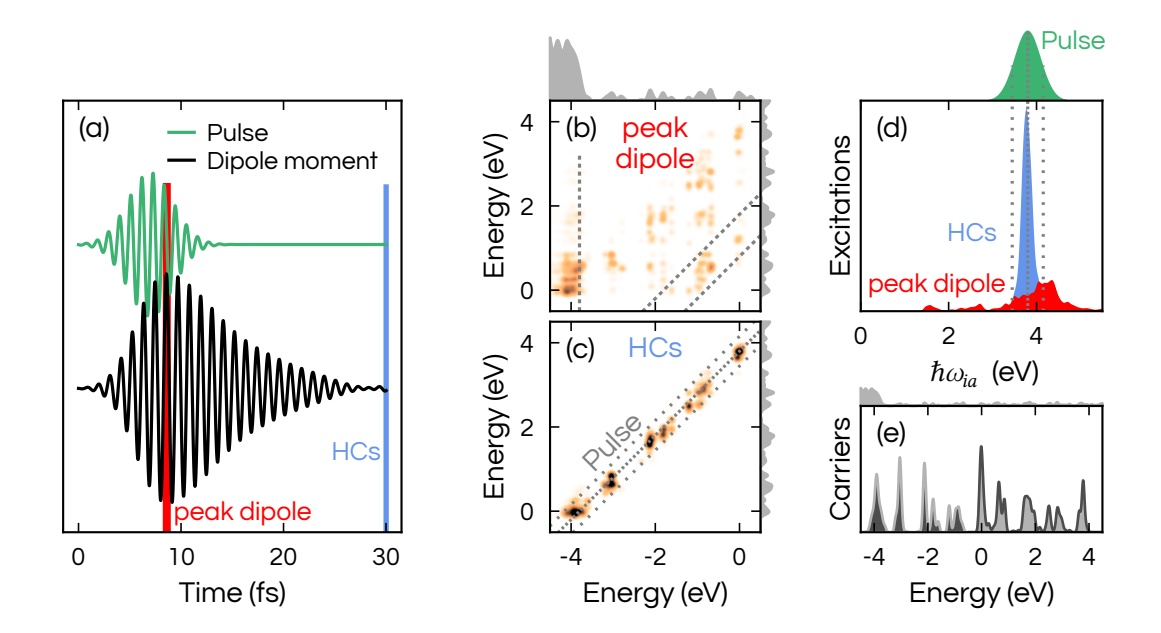


Figure 2.5: (a) Gaussian laser pulse and the resulting dipole moment induced in the NP. The time corresponding to the peak amplitude in the oscillating dipole moment is marked by a vertical bar and the label *peak dipole*. The final time in the simulation is marked by a vertical bar and the label *HCs*. (b-c) TCMs for the density matrix at the *peak dipole* (b) and *HCs* (c) time instances. The dashed lines in (b) are the same as in Fig. 2.4a and the dashed lines in (c) correspond to the center frequency and FWHM of the pulse. The scale of the colormap is identical in both panels. (d) Weighted sum of transitions Eq. (2.32) by transition energy $\hbar\omega_{ia}$ at the *peak dipole* and *HCs* time instances. (e) HCs $\hbar\omega_{ia}$ distribution at the *HCs* time instance.

through the effective coupling M_{ia} to the external field

$$P_{ia} \sim \left| M_{ia} \cdot E(\omega_{ia}) \right|^2. \tag{2.33}$$

This is similar to Fermi's golden rule type results that can be derived from other types of theory [28].

I have also plotted the distribution of holes $\sum_i G(\varepsilon - \varepsilon_i) P_i^{\text{hole}}$ and electrons $\sum_a G(\varepsilon - \varepsilon_a) P_a^{\text{electron}}$ at the final time in the simulation Fig. 2.5e. Because the hot electron (HE) and hot hole (HH) distributions are integrals of the TCM, the hottest electron that can be produced is one at $\hbar\omega_0 = 3.8$ eV (the corresponding hole is at the Fermi level) and the hottest hole is one at $-\hbar\omega_0 = -3.8$ eV (the corresponding electron is at the Fermi level). The HC distributions in this small NP consist of discrete peaks in the entire energy range between $\pm\hbar\omega_0$, but for larger NPs the HC distributions would approach that of bulk [15, 29, 30]. Theoretical predictions for extended surfaces [28, 31] and large NPs [29, 30] show two distinct regimes; for $\hbar\omega_0$ larger than the d-band onset, transitions from the d-band to the sp-band dominate, meaning that the holes are at least as hot as the d-band onset

(close to 2 eV for Au and Cu) while the electrons have relatively low energies [30]. In Ag (d-band onset almost 3.8 eV) this effect is most extreme, where a single peak in the HH distribution at the d-band, and a corresponding peak just above the Fermi level in the HE distribution, dominate. For $\hbar\omega_0$ below the d-band onset only sp-intraband transitions are possible, which generally results in broad HC distributions.

In order to utilize the HCs for technological applications, they need to be extracted out of the NP. The HCs lose energy through scattering with other electrons and with phonons. Some reports in the literature suggest that the time scale of equilibration is 100 fs to 1 ps for the former and several ps for the latter [13, 32–34]. Others, however, put the electron–phonon scattering rates to similar short time scales as electron–electron rates [28]. In either case, the HC distribution computed with RT–TDDFT about 20 fs after the center of the pulse, can be considered realistic for at least a few tens of fs.

2.3 Controlling hot-carrier generation

There are many demonstrations of HCs being useful for energy harvesting applications. By sandwitching plasmonic NPs between traditional electron- and hole extraction materials, a photovoltaic device can be created [35]. In such a device, HCs are generated due to the decay of the LSP and rapidly extracted by the corresponding material, to drive a photocurrent. A similar working principle has also been used to extract holes from Au NPs to partake in redox reactions of fuels [36, 37]. The role of the NPs can either be to make the electrically driven reaction selective towards one type of fuel [36], or to drive the reaction without any external bias [38]. There are also plenty of examples of NP-only (no electron or hole–collection materials) plasmonic catalysts of commercially important reactions [39–45]. It is generally thought that orbitals of a reactant molecule are transiently occupied by a HC, which puts the molecule in an excited state [46, 47]. The energy of the excited state is not necessarily high enough to force the chemical reaction of interest, but the reaction barrier is lowered enough to be able to be overcome by thermal vibrations.

There are two distinct processes in which HCs are thought to be injected to molecules [46]. In indirect HC transfer, HCs are injected after formation [42, 48, 49]. Due to the short lifetimes and mean free paths (few tens of nm [28, 49]) of HCs the window for injection is short in this process. In direct HC transfer [14, 39, 50, 51] on the other hand, the initial electron—hole pair to be created by the LSP decay consists of one carrier in the NP and the other in the molecule.

2.3.1 Spatial and energetic control of hot holes

I have shown in Sect. 2.1 (specifically Fig. 2.2b-c) that local alloying has a large effect on the d states due to their localized character. This promises an opportunity for control-

ling the spatial localization (by alloying in the desired location) and energy distribution (by choosing the alloy species) of HHs. The late transition metals have many more occupied d states than occupied s states, so it should be expected that control over the d state energies would have an impact on the efficacy of HC devices. However, alloying coinage metal NP (Ag, Au, Cu) with less noble metals (for example Pt, Pd, Ru, Rh, and Re) broadens the LSP [52–54] and leads to less absorbed power. Based on these ideas, there have been experimental realizations of alloyed or multicomponent nanostructures for catalytic purposes [40, 45, 55–57]. These systems consist of a large coinage metal part where the LSP forms, and a small amount of alloy elements. They have shown considerable improvements of catalytic activity compared to single–component systems.

In **Paper I** a systematic study of the effect of surface alloying on HH distributions was carried out. A series of Ag NPs with varying concentrations of Au, Cu, Pt, Pd, Ru, Rh, and Re alloyants in the surface was studied using RT–TDDFT. In the calculations, a Gaussian laser pulse was simulated, with its frequency tuned to the LSP $\hbar\omega_0=3.3\,\mathrm{eV}$, and the HC distributions after LSP decay were computed⁶.

These systems show an increase in the number of holes and a decrease in the number of electrons at the surface, as the surface Pt concentration is increased (Fig. 2.6a). The most drastic increase in holes occurs at low concentrations – a doubling of their number between 0 and 17 %. The largest number of holes in the surface is generated for a surface alloy concentration of 75 % and amounts to almost three times the value in pure Ag. Further increase of the concentration up to 100 % then decreases the number of holes, and the effect is not solely explained by a reduced absorption due to the broadening of the LSP. The reduced generation of electrons is less dramatic, but this effect is also not solely explained by the reduced absorption. It is also possible to control the energies of HHs by alloying. The dependence of HH energies shown in Fig. 2.6b clearly mirrors the dependence of the energetic position of the d–band on the alloy species (Fig. 2.2c). The hottest holes are obtained using Au as alloyant with the coldest holes for Re.

The observations can be explained in the light of the previous section. The total number of holes in the surface is obtained as a sum over occupied and unoccupied states i and a

$$N_{\rm HC} = \sum_{ia} P_{ia} w_{ia} \tag{2.34}$$

$$\sim \sum_{ia} |M_{ia} \cdot E(\omega_{ia})|^2 w_{ia}, \qquad (2.35)$$

where Eq. (2.33) was used in the second line and w_{ia} is a weight that quantifies whether the transition should be counted to the surface or not⁷. The factor $E(\omega_{ia})$ limits the largest (negative) value for the occupied states in the sum to the frequency of the pulse, which is 3.3 eV. Then, the holes in the Ag d-band can not be excited, but introducing Pt

⁶It should be noted that here the NPs are elongated along the polarization direction, and as such the LSP is redshifted compared to the NP studied in Sect. 2.2.3.

⁷More precise definitions are given in Paper I and Paper II.

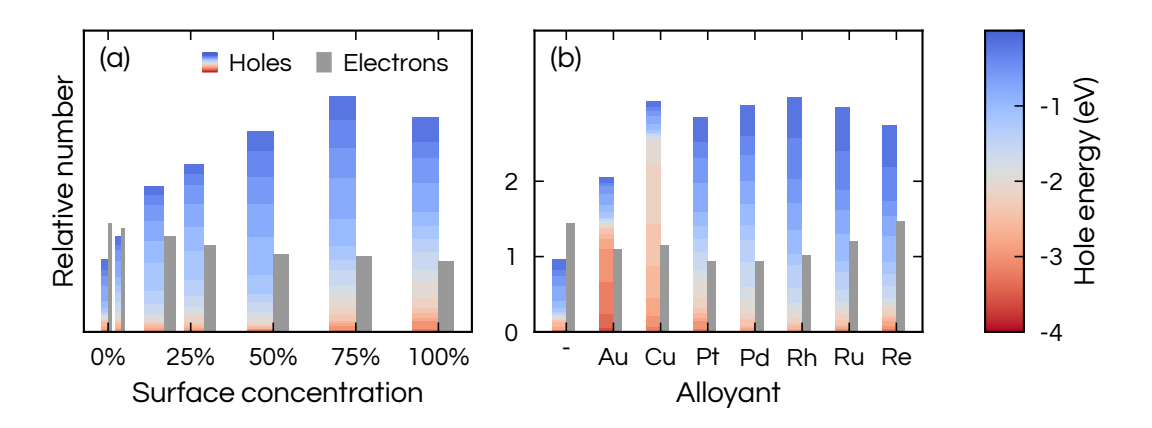


Figure 2.6: HH distributions in the NP surface as (a) the surface concentration of Pt increases and (b) as the alloy species is varied at a fixed 100% surface concentration. For the holes, the energetic distribution is shown as colored segments and the total height of the bar is proportional to the number of holes. For the electrons, bars proportional to the number of electrons are shown in grey.

provides d states 1-2 eV below the Fermi level (Fig. 2.2b), which are within reach of the pulse. The same principle applies for the other alloy species. This explains the drastic increase of HH at low concentrations. At higher alloyant concentrations the increase saturates and eventually decreases. The reduction of absorption $|E(\omega_{ia})|^2$ due to the broader LSP only partially explains the reduction. Instead, it must be that the coupling strength M_{ia} is reduced, either by a change in the field of the LSP, or due to screening by the other transitions from d states. The conclusion of Paper I is that small amounts of alloyant, even less than one full surface layer are most effective for HC generation. The same conclusion has been also been drawn from semi-classical calculations of larger NPs in Ref. [52].

2.3.2 Increasing the probability of direct transfer

Paper II is focused on the direct HC transfer process. Then, it is relevant to count the number of transitions from an occupied state i localized to the NP to an unoccupied state a localized to a nearby molecule (or the opposite transition). Equation (2.35) applies here as well, where w_{ia} is now a weight that quantifies whether it is such a charge-transfer transition. RT-TDDFT calculations with a Gaussian laser were performed for a Ag NP (the same isotropic one as in Sect. 2.2.3) and a CO molecule. A range of distances between NP and molecule were considered, along the approach to the high symmetry site in the middle of the (111) face. The idea is to inject electrons to the lowest unoccupied molecular orbital (LUMO) of the molecule, which is about 2.8 eV above the Fermi level of

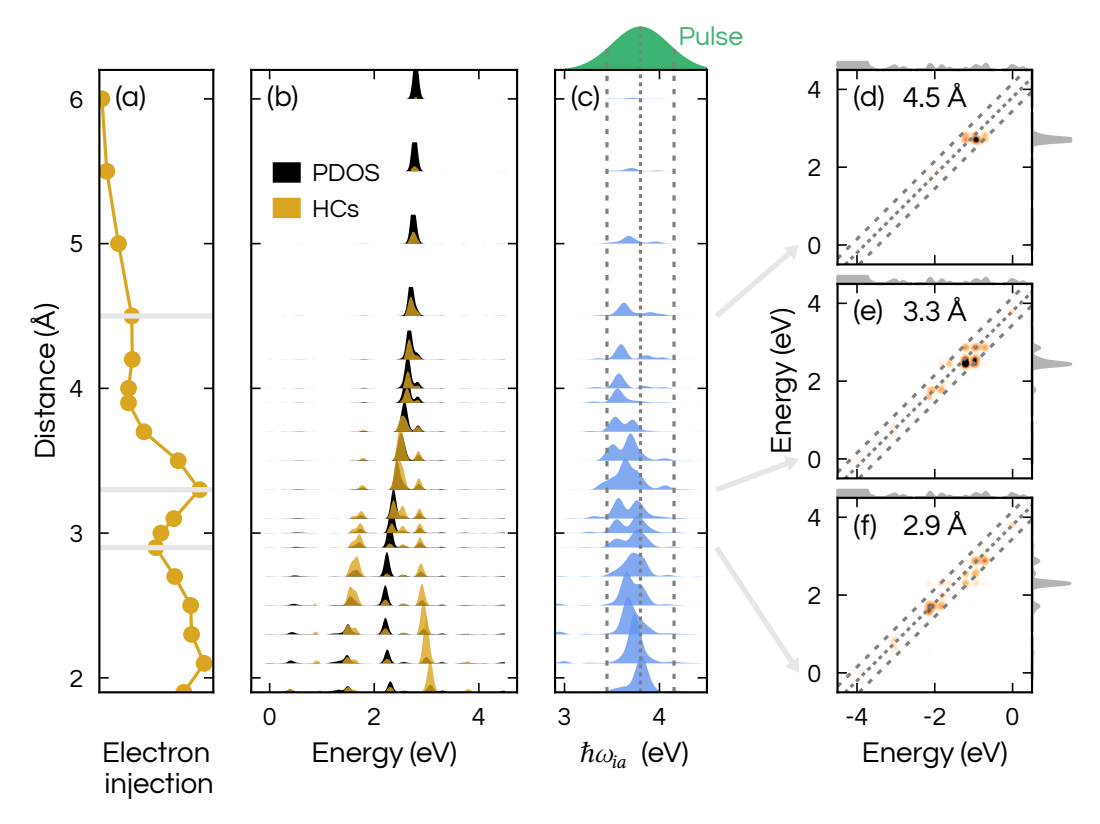


Figure 2.7: (a) Relative number of electrons injected into the CO molecule after resonant excitation, as a function of distance between the NP and molecule. (b) PDOS of the molecule and HE distribution corresponding to transitions to the molecule, for various distances. (c) Weighted transition probability of charge—transfer excitations Eq. (2.37). The dashes lines indicate the center frequency and FWHM of the pulse in the frequency domain. (d–f) TCMs for charge—transfer excitations for selected distances.

the metal when the systems are far separated. The highest occupied molecular orbital (HOMO) is too far from the Fermi level for hole injection from Ag to CO to be possible.

The relative number of electrons injected into the molecule after LSP decay is shown in Fig. 2.7a, for a driving laser tuned in resonance the to the LSP (3.8 eV). This quantity depends non-monotonically on the distance between NP and molecule, in the range of 2 to 4.5 Å. In fact, the maximum occurs at a distance of 3.3 Å, which is outside the binding energy well (see Paper II for binding energy calculations), suggesting that adsorption is not strictly necessary for HE transfer. At further distances, the charge transfer decreases monotonically until it reaches zero at 6 Å. This, perhaps unintuitive, behavior can be explained using the tools introduced in the previous parts of this chapter.

From a plot of the molecular PDOS (Fig. 2.7b) it is seen that the LUMO hybridizes with the metal as the distance is decreased. The energy shifts closer to the Fermi level,

starting from 2.8 eV at far distances. Around 4 Å, it splits into several states due to hybridization with many metal states. It should be noted, that the DOS of the NP is practically independent of distance, due to the much larger size of the NP. A HE distribution projected on the molecule

$$\sum_{ia} P_{ia} w_{ia} G(\hbar \omega_{ia} - \hbar \omega) \tag{2.36}$$

is calculated and plotted together with the PDOS. It seems then, that the projected HE distribution is redistributed between the several hybridized peaks in the PDOS as the distance is varied. For example, at 3.3 Å, which is the maximum of injection, the middle of the three prominent peaks has the most electrons, but at 3.1 Å the electrons are almost uniformly spread out over the peaks in the PDOS.

The answer to this puzzling behavior lies in the interplay between the coupling strength M_{ia} and the factor $E(\omega_{ia})$ in Eq. (2.35). Because the weight w_{ia} is non zero only for excitations to the molecule, and there are few available states in the molecule (one LUMO which is split into a few states due to hybridization), then few states a are contributing to the sum Eq. (2.35). The donor states i in the NP which are energetically aligned in order to fulfill the alignment criterion (large values of $E(\omega_{ia})$, meaning $\omega_{ia} \sim \omega_0$), do not necessarily have large coupling strength M_{ia} , and vice versa. This can be illustrated by plotting the weighted sum of charge—transfer excitations by transition energy

$$\sum_{ia} P_{ia} w_{ia} G(\varepsilon_a - \varepsilon) \tag{2.37}$$

in Fig. 2.7c. The electron-transfer transitions are for most distances not aligned to the pulse, but slightly redshifted to it. By contrast, excitations for the system as a whole are resonant with the pulse (Fig. 2.5d), because there are more combinations of possible states that simultaneously have large values of M_{ia} and $E(\omega_{ia})$.

Yet another visualization of the excitations, is to simply plot the TCMs of $P_{ia}w_{ia}$ at a few selected distances (Fig. 2.7d-f). The transitions occur at points where the molecular PDOS intersects the NP DOS for the combination of states with the most significant values of M_{ia} . While the alignment criterion selects excitations close to resonance, many excitations fall anywhere within the FWHM of the pulse. With these observations, it can be concluded that the non-monotonic distance dependence of electron injection is a consequence of the more efficient (larger M_{ia}) excitations falling in and out of resonance due to shifts in the PDOS.

In the alignment criterion Eq. (2.35), the exciting laser frequency acts as a handle determining the energetic difference between generated electrons and holes. Transitions that are misaligned to the pulse can be aligned by changing the pulse frequency. This hypothesis is tested by mapping out the HE transfer on distance and laser frequency (Fig. 2.8a). While the energy absorbed decreases by detuning the laser from the LSP resonance, the absolute maximum of electron transfer occurs around 3.6 eV. The trend seems to be quite consistent across the different distances. Then, focusing only on the

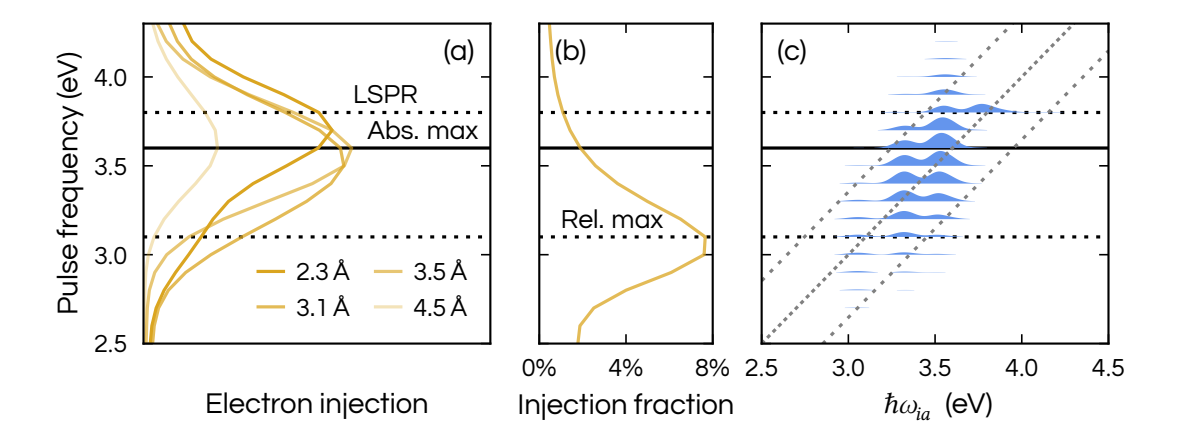


Figure 2.8: (a) Relative number of electrons injected into the CO molecule, for selected distances between the NP and molecule, as a function of laser frequency. (b) The fraction of electrons injected for the distance 3.1 Å. (c) Weighted transition probability of charge—transfer excitations Eq. (2.37), by laser frequency, for the distance 3.1 Å. The horizontal lines in the plot indicate the LSP resonance at 3.8 eV, the absolute maximum of electron injection (for most distances) at 3.6 eV, and the relative maximum (in other words the maximum of the injection fraction) of the electron injection normalized by the number of carriers in total at 3.1 eV (for the distance 3.1 Å).

 $3.1\,\text{Å}$ distance, an injection fraction is computed (Fig. 2.8a). This quantity is the number of injected electrons, divided by the number of electrons excited in the system as a whole (the latter being roughly proportional to the amount of energy absorbed). This quantity reaches $8\,\%$ at this particular distance, for laser frequencies of $3-3.1\,\text{Å}$, which should be compared to the value $2\,\%$ for a laser tuned to the LSP.

Paper II shows that the direct HC transfer process can be effective, and that it is sensitive to the electronic structure of the hybridized molecular orbitals. In terms of numbers, the observations in Paper II are specific to this particular system (and even to the site of approach). However, the underlying physics are general, and it should be expected that all similar systems can potentially suffer from this misalignment between the frequency ω_{ia} of the most effective charge transfer excitations, the frequency of the laser ω_0 and the LSP resonance. For practical applications, it might be of interest to excite the system by solar light, instead of a narrow–band laser pulse. Still, a misalignment between ω_{ia} and the LSP resonance might remain. There is potentially a chance of improving the efficiency of a HC device by modifying its absorption spectrum, for example by changing shape or embedding in dielectric materials [58]. Another, non intrusive way, utilizing strong coupling is presented in the next chapter.

Strong coupling

In the regime of strong light—matter coupling, the behavior of coupled systems is different not only quantitatively, but also qualitatively, to the weakly coupled case. The most sophisticated models of strong coupling (SC) belong to the formalism of quantum electrodynamics [7] but the basic ideas are seen already in simple classical models of coupled harmonic oscillators [59]. In the first part of this chapter, I show how SC emerges, starting from a model of two coupled harmonic oscillators. This model is applicable both for electronic transitions and vibrational motion, which is why SC can occur both in the visible (coupling to electronic transitions) [60, 61] and infrared (coupling to nuclear motion) domains [62–64].

There are promising opportunities for improving sensing [61] and catalysis [62] with SC, but the mechanisms behind observed improvements are not fully understood [65]. In the last part of this chapter, I focus on efficient theoretical methods for studying SC in Papers III, IV and V.

3.1 Principles of strong coupling

In typical experiments where SC between molecules and light is observed, one takes molecules that have a clearly peaked optical spectrum at ω_0 , confines them in an optical cavity, and measures the optical spectrum [60]. The cavity should be tuned so that its resonance frequency is close to ω_0 . If SC occurs, the ω_0 peak splits into two peaks (Fig. 3.1). The two peaks correspond to hybrid light-matter states called polaritons, the lower polariton (LP) having frequency $\Omega_- < \omega_0$ and the upper polariton (UP) $\Omega_+ > \omega_0$.

The confinement of the light to a small mode volume inside the cavity is responsible for increasing the strength of the coupling between the molecular transition and the electric field, which is otherwise very weak in the absence of a cavity. In theory, one can

imagine turning the coupling strength g between the molecule and the field up from zero to a high value. This is demonstrated later in this chapter. Initially there is an increase in amplitude seen in the spectrum of the molecule (Fig. 3.1). This is known as the Purcell effect and characteristic of weak coupling [7]. Eventually the peak splits in two polaritons, a signature of SC, the quantity $\Omega_R = \Omega_+ - \Omega_-$ being known as Rabi splitting. SC is typically taken to be when the Rabi splitting is larger than the linewidth $\Omega_R > \eta$ [66], where η is the linewidth.

No matter whether classical matter-classical light, quantum matter-classical light or quantum matter-quantum light models are considered, theory predicts [66]

$$\Omega_R \sim \sqrt{N/V}$$
. (3.1)

The certain means for increasing the coupling strength are thus to confine the light to a smaller volume V, and to increase the number of molecules N that collectively couple to the cavity.

In quantum models such as the Jaynes–Cummings two–state model [66, 67], g is a direct measure of the coupling strength between the electromagnetic (EM) field and matter. At resonance of the molecule and cavity, the Rabi splitting is related to g and the linewidths as

$$\Omega_R = \sqrt{4g^2 - (\eta_{\text{molecule}} - \eta_{\text{cavity}})^2}.$$
 (3.2)

The coupling strength is in turn obtained from the transition dipole moment μ and the vacuum field strength

$$\hbar g = \sqrt{N} \mu E_{\text{vac}} \tag{3.3}$$

$$\hbar g = \sqrt{N} \mu E_{\text{vac}}$$

$$E_{\text{vac}} = \sqrt{\frac{\hbar \omega_0}{2\epsilon_0 V}}.$$
(3.3)

Coupled harmonic oscillators 3.1.1

The key characteristics of SC can be illustrated by studying classical coupled harmonic oscillators [59]. The following equation describes the motion of a damped harmonic oscillator with a displacement coordinate *x*:

$$\ddot{x}(t) + 2\eta \dot{x}(t) + \omega_0^2 x(t) = C \cdot E(t). \tag{3.5}$$

The oscillator could represent for example a localized surface plasmon (LSP) or an electronic transition. This model is even more simplistic than the small sphere of a freeelectron metal in Sect. 2.2.1, but the form can be phenomenologically motivated; the second term is responsible for a friction that slows down the velocity \dot{x} and the third term describes a restoring force to the displacement x. The constant η is the strength

of the friction, and ω_0 is the resonance frequency of the oscillator in the absence of friction. The oscillator is driven by the electric field E(t) with proportionality constant C. The same constant can also be assumed to relate the displacement to the dipole moment

$$\mu(t) = Cx(t). \tag{3.6}$$

Taking the Fourier transform (defined in Eq. (4.18)) of Eq. (3.5) and rearranging the terms yields the polarizability of the system

$$\alpha(\omega) = \frac{Cx(\omega)}{E(\omega)} = -\frac{C^2}{(\omega + i\eta)^2 - \bar{\omega}_0^2},\tag{3.7}$$

where $\bar{\omega}_0^2 = \omega_0^2 - \eta^2$. A polarizability of the form Eq. (3.7) is called a Lorentzian, and the corresponding absorption $\sim \omega \cdot \text{Im } \alpha$ has a maximum at $\bar{\omega}_0$.

Now, two harmonic oscillators 1 and 2 that are coupled through their velocity are considered [59]. The equations of motion are

$$\ddot{x}^{(1)}(t) + 2\eta_1 \dot{x}^{(1)}(t) + \omega_1^2 x^{(1)}(t) + 2g\dot{x}^{(2)}(t) = C_1 \cdot E(t)$$
(3.8)

$$\ddot{x}^{(2)}(t) + 2\eta_2 \dot{x}^{(2)}(t) + \omega_2^2 x^{(2)}(t) - 2g\dot{x}^{(1)}(t) = C_2 \cdot E(t). \tag{3.9}$$

The only difference from Eq. (3.5) is the additional coupling of strength $\pm 2g$ to the velocity of the other oscillator. The coupled system needs to be considered to find the solution, which is conveniently expressed as the matrix equation

$$\begin{bmatrix} 1 & 0 \\ 0 & 1 \end{bmatrix} \begin{bmatrix} \ddot{x}^{(1)}(t) \\ \ddot{x}^{(2)}(t) \end{bmatrix} + 2 \begin{bmatrix} \eta_1 & g \\ -g & \eta_2 \end{bmatrix} \begin{bmatrix} \dot{x}^{(1)}(t) \\ \dot{x}^{(2)}(t) \end{bmatrix} + \begin{bmatrix} \omega_1^2 & 0 \\ 0 & \omega_2^2 \end{bmatrix} \begin{bmatrix} x^{(1)}(t) \\ x^{(2)}(t) \end{bmatrix} = \begin{bmatrix} C_1 \\ C_2 \end{bmatrix} \cdot E(t).$$
 (3.10)

Taking the Fourier transform and introducing the denominators of the Lorentzians

$$L_1 = (\omega + i\eta_1)^2 - (\omega_1^2 - \eta_1^2)$$
(3.11)

$$L_2 = (\omega + i\eta_2)^2 - (\omega_2^2 - \eta_2^2), \tag{3.12}$$

yields the matrix equation

$$\underbrace{\begin{bmatrix} -L_1 & -2i\omega g \\ 2i\omega g & -L_2 \end{bmatrix}}_{A(\omega)} \underbrace{\begin{bmatrix} x^{(1)}(\omega) \\ x^{(2)}(\omega) \end{bmatrix}}_{x(\omega)} = \underbrace{\begin{bmatrix} C_1 \\ C_2 \end{bmatrix}}_{C} E(\omega).$$
(3.13)

The inverse of the matrix *A* can be used to obtain the displacements of the individual oscillators

$$\mathbf{x}(\omega) = \mathbf{A}^{-1}(\omega) C E(\omega) \tag{3.14}$$

$$A^{-1}(\omega) = \frac{1}{\det A} \begin{bmatrix} -L_2 & 2i\omega g \\ -2i\omega g & -L_1 \end{bmatrix}$$
 (3.15)

$$\det \mathbf{A}(\omega) = L_1 L_2 - 4\omega^2 g^2. \tag{3.16}$$

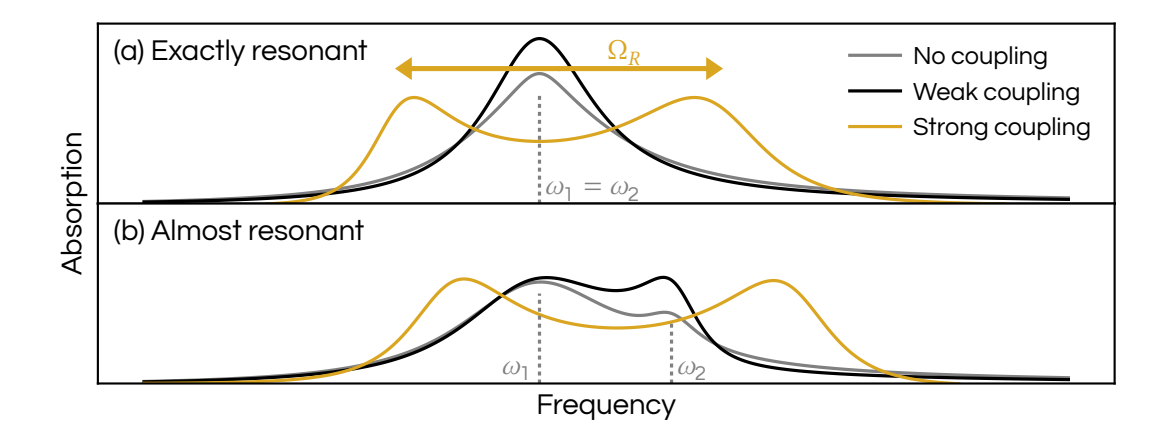


Figure 3.1: Absorption spectrum of uncoupled, weakly coupled and strongly coupled harmonic oscillators in the (a) exactly resonant and (b) almost resonant cases. The almost resonant case shows clearly how the intensity of the higher frequency oscillator, which is small in the uncoupled case, is greatly enhanced for weak coupling (Purcell effect). For SC, Rabi splitting is clearly visible.

The sum of the individual dipole moments is the total dipole moment, and can be written $C^T x$. Then, the polarizability of the coupled system is

$$\alpha(\omega) = C^T A^{-1}(\omega) C. \tag{3.17}$$

I have plotted the absorption (Eq. (4.28)) corresponding to the polarizability Eq. (3.17) for an exactly resonant ($\omega_1 = \omega_2$), and an almost resonant ($\omega_2 = 1.2 \cdot \omega_1$) system in Fig. 3.1a and Fig. 3.1b, respectively. In these plots, the amplitudes are $C_1 = 10 \cdot C_2$ and the widths $\eta_1 = \eta_2 = 0.1 \cdot \omega_1$. For a weak coupling strength $g = 0.1 \cdot \omega_1$, both plots show an increase in amplitude compared to no coupling g = 0, while the resonances remain in their original positions. This is known as the Purcell effect. Choosing instead a large coupling strength $g = 0.5 \cdot \omega_1$, the peaks in the spectra shift to new positions, which is known as Rabi splitting.

By making a few more assumptions, useful relations can be derived from Eq. (3.17). Often, one of the systems couples much more strongly to the driving field than the other $(C_1 \gg C_2)$, for example if oscillator 1 is a cavity and oscillator 2 a small molecule. This motivates setting $C_2 = 0$. Then the polarizability is

$$\alpha(\omega) = -\frac{C_1^2 L_2}{L_1 L_2 - 4\omega^2 g^2}$$

$$= -\frac{C_1^2 \left(\omega^2 + 2i\eta_2 - \omega_2^2\right)}{\left(\omega^2 + 2i\eta_1 - \omega_1^2\right) \left(\omega^2 + 2i\eta_2 - \omega_2^2\right) - 4\omega^2 g^2}.$$
(3.18)

$$= -\frac{C_1^2 \left(\omega^2 + 2i\eta_2 - \omega_2^2\right)}{\left(\omega^2 + 2i\eta_1 - \omega_1^2\right) \left(\omega^2 + 2i\eta_2 - \omega_2^2\right) - 4\omega^2 g^2}.$$
 (3.19)

If the two oscillators are exactly resonant $\omega_1 = \omega_2 = \omega_0$, the denominator can be factorized with some algebra, so that

$$\alpha(\omega) = -\frac{C_1^2 L_2}{L_+ L_-} \tag{3.20}$$

$$=\frac{C_1^2 L_2}{2\omega\Omega_R} \cdot \left(\frac{1}{L_-} - \frac{1}{L_+}\right),\tag{3.21}$$

where the following quantities have been introduced:

$$L_{+} = \omega^2 + \omega(2i\bar{\eta} + \Omega_R) - \omega_0^2 \tag{3.22}$$

$$L_{-} = \omega^2 + \omega(2i\bar{\eta} - \Omega_R) - \omega_0^2 \tag{3.23}$$

$$\bar{\eta} = (\eta_1 + \eta_2)/2 \tag{3.24}$$

$$\Omega_R = \sqrt{4g^2 - (\eta_1 - \eta_2)^2} \tag{3.25}$$

The expression Eq. (3.21) shows that the polarizability approximately behaves like the difference of $1/L_{-}$ and $1/L_{+}$. This form makes the distinction between the weak and strong coupling regimes clear. Weak coupling occurs in the coupled oscillator model for $2g < |\eta_{1} - \eta_{2}|$. Then $\Omega_{R} = i\sqrt{(\eta_{1} - \eta_{2})^{2} - 4g^{2}}$ is purely imaginary so that

$$L_{\pm} = \omega^2 + 2i\omega \left(\bar{\eta} \pm \sqrt{(\eta_1 - \eta_2)^2 / 4 - g^2}\right) - \omega_0^2$$
 (3.26)

are the denominators of Lorentzians with resonance frequency ω_0 and a linewidth that is changed compared to the uncoupled oscillators, according to the expression in the bracket.

Strong coupling occurs in the coupled oscillator model for $2g>|\eta_1-\eta_2|$. Then, the expression Eq. (3.25) for Ω_R is purely real and identical to the expression for Rabi splitting as in the Jaynes–Cummings model Eq. (3.2). Then, $1/L_\pm$ are approximately Lorentizans with linewidth $\bar{\eta}$ and center frequencies $\omega_0=\sqrt{\omega_0^2+\Omega_R^2/4}\pm\Omega_R/2$, corresponding to a slight blue–shift of both peaks and splitting by Ω_R . The coupled oscillator model thus recovers the traditional Rabi splitting expression.

3.2 Exploiting strong coupling

SC has been successfully exploited to modify chemical and photochemical properties, by coupling either electronic [60, 61] or vibrational [62–64] degrees of freedom to confined EM modes. However, computational models that accurately reproduce experiments are scarce, as the complexity of models grows large when electronic, nuclear, and EM degrees of freedom need to be included. Additionally, SC is known to be able to form polaritonic states delocalized over hundreds of thousands of molecules [7], which means

that potentially large numbers of moieties need to be included. The common theme in Papers III, IV and V is thus to find efficient models while keeping the detailed description of matter.

3.2.1 Dipolar coupling

In **Paper III**, a method based on dipolar coupling (DC) of subsystems is derived in order to study SC. The method relies on time-dependent density-functional theory (TDDFT) (or other theory) input in the form of polarizabilities of individual subsystems, e.g., molecules and nanoparticles (NPs), but is otherwise computationally very cheap even for large ensembles. The goal of the DC method is to find a macroscopic polarizability $\alpha(\omega)$ of the entire ensemble, expressed in the positions and polarizabilities of the individual subsystems. This macroscopic polarizability is defined as the proportionality constant between the external electric field $E_{\rm ext}$ applied to the system and the total dipole of the system (repeated in Eq. (4.26))

$$\mu(\omega) = \alpha(\omega) E_{\text{ext}}(\omega). \tag{3.27}$$

The method is considered in the electric dipole approximation, which is valid when the system is smaller than the relevant wavelengths of light. Then, retardation effects are neglected and the field responds instantaneously to changes in the charge density. The external field $E_{\rm ext}$ is taken to be spatially uniform (the same is, however, not true for the internal fields in the ensemble).

In the DC method, N subsystems enumerated 1, 2, ..., N are considered. It is assumed that the only interaction between subsystems is that of interacting point dipoles. Each subsystem i has a polarizability $\alpha^{(i)}$ that relates the total electric field at the position $r^{(i)}$ of the unit $E_{\text{tot}}^{(i)}(\omega) = E_{\text{tot}}(r^{(i)}, \omega)$ to the dipole of the unit

$$\boldsymbol{\mu}^{(i)}(\omega) = \boldsymbol{\alpha}^{(i)}(\omega) E_{\text{tot}}^{(i)}(\omega). \tag{3.28}$$

This polarizability encodes all materials properties of the subsystem. For simplicity, it is assumed that the subsystems are charge neutral. Thus the total dipole moment of the ensemble is obtained by summation

$$\mu(\omega) = \sum_{i=1}^{N} \mu^{(i)}(\omega). \tag{3.29}$$

The total electric field at each unit consists of a contribution from an external electric field $E_{\rm ext}(\omega)$ and the field due to the dipoles of other units. Inserting the distance vector $\mathbf{r}^{(ij)} = \mathbf{r}^{(i)} - \mathbf{r}^{(j)}$ into Eq. (4.25), the field at the position of unit i due to the dipole of unit j reads

$$T^{(ij)}\boldsymbol{\mu}^{(j)},\tag{3.30}$$

where the coupling is

$$T^{(ij)} = \frac{1}{4\pi\varepsilon_0} \left(\frac{3\mathbf{r}^{(ij)}(\mathbf{r}^{(ij)})^{\mathrm{T}}}{|\mathbf{r}^{(ij)}|^5} - \frac{1}{|\mathbf{r}^{(ij)}|^3} \right).$$
(3.31)

The coupling matrices $T^{(ij)}$ are frequency independent due to the neglect of retardation, which is a convenient simplification. The equations above can be summarized by the following equation for the tensors $\mu(\omega)$, $\underline{\alpha}_0(\omega)$, $\underline{E}_{\rm tot}(\omega)$ and $\underline{E}_{\rm ext}(\omega)$

$$\begin{bmatrix}
\mu^{(1)}(\omega) \\
\mu^{(2)}(\omega) \\
\vdots \\
\mu^{(N)}(\omega)
\end{bmatrix} = \begin{bmatrix}
\alpha^{(1)}(\omega) \\
\alpha^{(2)}(\omega) \\
\vdots \\
\alpha^{(N)}(\omega)
\end{bmatrix}
\underbrace{\begin{bmatrix}
E_{tot}^{(1)}(\omega) \\
E_{tot}^{(2)}(\omega) \\
\vdots \\
E_{tot}^{(N)}(\omega)
\end{bmatrix}}_{\underline{\mu}(\omega)}$$

$$(3.32)$$

$$\underline{\mu}(\omega) \qquad \underline{\underline{\alpha}_{0}}(\omega) \qquad \underline{\underline{E}_{tot}}(\omega)$$

$$\underline{F}_{tot}^{(1)}(\omega) \qquad \underline{\underline{\Gamma}_{tot}}(\omega) \qquad \underline{\underline{\Gamma}$$

$$\underbrace{\frac{\boldsymbol{\mu}(\omega)}{E_{\text{tot}}^{(1)}(\omega)}}_{\underbrace{E_{\text{tot}}^{(2)}(\omega)} = \underbrace{\begin{bmatrix} E_{\text{ext}}(\omega) \\ E_{\text{ext}}(\omega) \\ \vdots \\ E_{\text{ext}}(\omega) \end{bmatrix}}_{\underline{E}_{\text{ext}}(\omega)} + \underbrace{\begin{bmatrix} 0 & T^{(12)} & \dots & T^{(1N)} \\ T^{(21)} & 0 & T^{(2N)} \\ \vdots & \ddots & \vdots \\ T^{(N1)} & T^{(N2)} & \dots & 0 \end{bmatrix}}_{\underline{E}_{\text{ext}}(\omega)} \underbrace{\begin{bmatrix} \boldsymbol{\mu}^{(1)}(\omega) \\ \boldsymbol{\mu}^{(2)}(\omega) \\ \vdots \\ \boldsymbol{\mu}^{(N)}(\omega) \end{bmatrix}}_{\underline{\boldsymbol{\mu}}(\omega)}. \tag{3.33}$$

Having neglected retardation, the tensor for the external electric field consists of the same value $E_{\rm ext}(\omega)$ repeated. By substituting Eq. (3.33) into Eq. (3.32) and solving for the induced dipole moment, the dipole tensor is obtained

$$\mu(\omega) = \left[\underline{I} + \underline{\alpha}_0(\omega)\underline{T}\right]^{-1}\underline{\alpha}_0(\omega)\underline{E}_{\text{ext}}(\omega), \tag{3.34}$$

where \underline{I} is the identity tensor. The proportionality tensor is interpreted as a reducible subsystem—wise polarizability $\underline{\alpha}(\omega)$, which is obtained by solving the linear tensor equation

$$\left[\underline{I} + \underline{\alpha}_{0}(\omega)\underline{T}\right]\underline{\alpha}(\omega) = \underline{\alpha}_{0}(\omega). \tag{3.35}$$

The macroscopic polarizability is thus given by the double summation

$$\alpha(\omega) = \sum_{i}^{N} \sum_{j}^{N} [\underline{\alpha}]_{ij}(\omega). \tag{3.36}$$

The computationally most expensive part of the DC method is the solution of Eq. (3.35), which has to be done once for every frequency of interest. Generally, the DC method

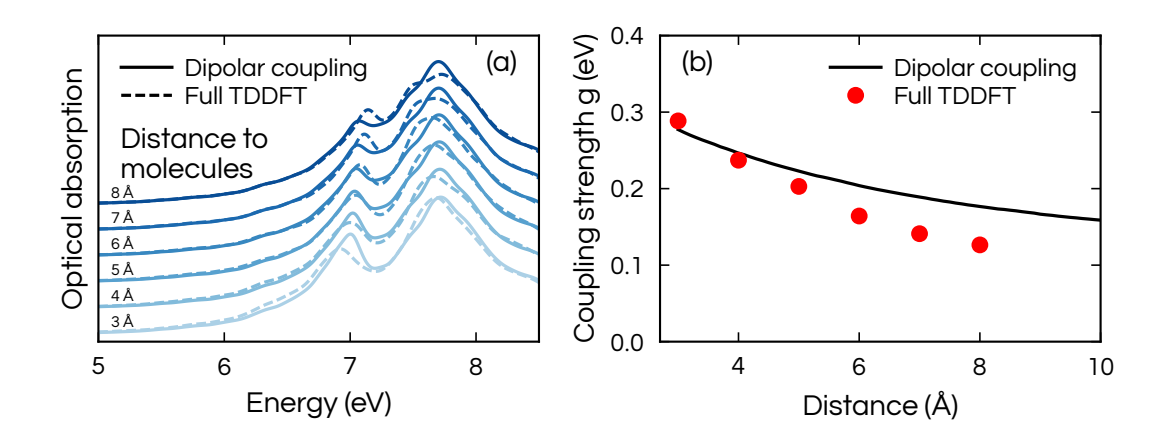


Figure 3.2: (a) Optical spectra for the coupled system of the Al NP and 2 benzene molecules with different separations to the molecules. The DC data is in good agreement to the reference TDDFT calculations. (b) Coupling strengths obtained by fitting a coupled oscillator model to the DC and TDDFT spectra. SC is achieved for small distances.

is still orders of magnitude faster than TDDFT calculations, as the size of the tensors in Eq. (3.35) scale with the number of subsystem, while the size of the system in TDDFT scales with the number of electrons. Generally, each subsystem in the DC method would be comprised of many electrons.

Using the DC method, I have computed the absorption spectrum for a system comprised of a 201-atom Al NP and two benzene molecules on each side. The NP has a LSP resonance at 7.7 eV, which is close to the first bright excitation of the molecule at 7.1 eV. Varying the distance between the molecules effectively modifies the coupling strength between the molecular excitation and the LSP. This effect is visible in the spectra as increased Rabi splitting of the LP with smaller distances (Fig. 3.2a). Fitting the obtained spectra to the coupled harmonic oscillator model Eq. (3.19) the relationship to the coupling strength is seen directly (Fig. 3.2b). The DC spectra are in good agreement with TDDFT spectra from Ref. [68] (Fig. 3.2). The most apparent differences in the spectra are at small distances, where the DC method underestimates the position of the LP. Such a shortcoming is to be expected at short distances, as the method does not allow the systems to hybridize, and neglects charge transfer and near field effects. In contrast to the spectra, the agreement in coupling strength g between TDDFT and DC becomes worse with increasing distance. This can be attributed to two effects: basis set superposition errors associated with localized basis sets in TDDFT lead to a blueshift of the LP at far distances (in turn underestimating g), while the lack of orbital hybridization in DC possibly underestimates g at short distances.

I also vary the number of molecules around the NP (keeping them at the distance of 3 Å). The agreement in spectra (Fig. 3.3a) and coupling strength (Fig. 3.3b) in comparison

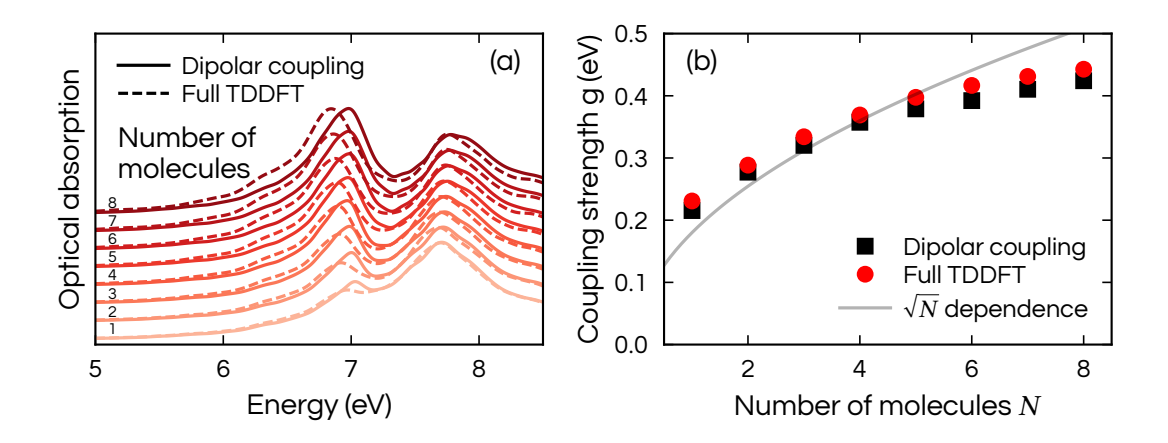


Figure 3.3: (a) Optical spectra for the coupled system of the Al NP and different numbers of benzene molecules and (b) corresponding coupling strength obtained from fits to a coupled oscillator model. The expected \sqrt{N} dependence is followed for small numbers of molecules, until it saturates. A line is included to guide the eye.

to the TDDFT results from Ref. [68] is good. Up to 4 molecules or so, the signature \sqrt{N} dependence of SC is obeyed, and the deviation for more than 4 molecules is the same in DC and TDDFT. Thus, the DC method efficiently and relatively accurately captures material specific response in the optical domain of SC.

3.2.2 Increasing hot-carrier generation

In Chapter 2, I have shown how the injection of electrons from a Ag NP into a CO molecule via the direct hot carrier (HC) transfer process is hindered by a trade-off. Light is most easily absorbed around the LSP resonance at 3.8 eV, while the transition energies of the most effective charge-transfer excitations are closer to 3 eV. Due to this trade-off, the highest probability of transfer, using a narrow-band laser, is achieved by choosing a laser frequency of 3.6 eV. In this chapter I have demonstrated that optical resonances can be shifted by strongly coupling to light. This suggests that it should be possible to engineer a red-shifted resonance and inject more electrons to the molecule.

In **Paper IV**, the Ag NP from Paper II is studied under the influence of an optical cavity. The NP and molecule are modeled using real-time time-dependent density functional theory (RT-TDDFT). They are placed in an optical cavity, which is modeled as one idealized cavity mode. Not unlike the dipolar coupling method in Sect. 3.2.1, there are two subsystems, the electronic system (which is described with RT-TDDFT) and the cavity mode (which is described as a classical harmonic oscillator with a mode coordinate Eq. (4.29)). Their interaction is through radiation-reaction, where the electronic dipole acts on the cavity, which produces a field Eq. (4.30) that acts back on the system. By re-

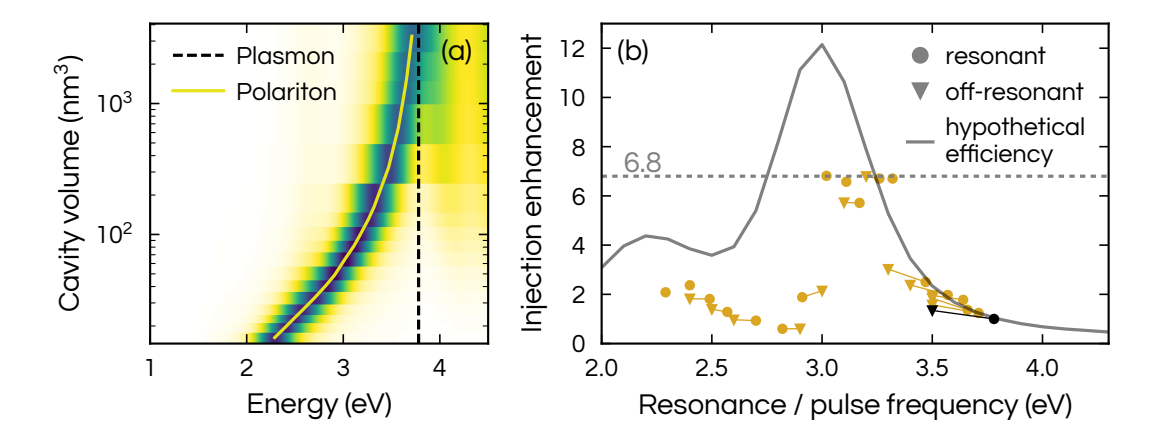


Figure 3.4: (a) Absorption spectrum of the Ag NP in an optical cavity. As the mode volume of the cavity is decreased from values above thousands of nm³, where there is effectively no coupling, the coupling strength increases and LP and UP appear. The energetic position of the LP resonance very closely follows the curve $3.805 \, \text{eV} - 6.2425 \, \text{eVnm}^{3/2} / \sqrt{V}$, where V is the cavity volume. (b) Enhancement of electron injection for different setups. Because the principal charge–transfer excitation is red–detuned relative to the LSP resonance, transferring the most charge requires a trade–off between being tuned to the resonance (circles) and being tuned to the charge–transfer excitation. The grey line is the injection for the no–cavity system, normalized by the absorbed energy at every different frequency.

ducing the cavity to one mode of a simple form, the computational cost of this method is no higher than the cost of the calculations in Paper II.

Across the different distances between the CO molecule and NP that were considered in Paper II, the general trend for charge–transfer as a function of pulse frequency was consistent. Therefore, Paper IV is focused the distance $3\,\text{Å}$ in particular. The cavity frequency $\hbar\omega_c=3.8\,\text{eV}$ is chosen to be resonant with the LSP, and the mode volume parameter V is varied¹. In reality, there are different ways of realizing such a cavity, including mirrors, bow–tie antennas [69], or picocavities [70], but the simple form of the cavity qualitatively captures the physics in all of these domains. As the mode volume is decreased, the absorption spectrum of the system (Fig. 3.4a) shows a splitting into LP and UP. The UP can be seen at large mode volumes in the plot, but becomes dark eventually, so that the only bright resonance of the system is the LP. It is of similar width to the LSP

¹It should also be noted that in these simulations, the external field was setup to directly effect only the matter subsystem, in order to decouple the analysis from the effect of increased of absorption cross section overall, due to the inclusion of the cavity.

in the cavity-free NP. The energetic position of the LP closely follows the fit

$$3.805 \,\text{eV} - \frac{6.2425 \,\text{eVnm}^{3/2}}{\sqrt{V}}.\tag{3.37}$$

The $1/\sqrt{V}$ -dependence of the Rabi splitting is to be expected given Eqs. (3.2)–(3.4).

The enhancement in injection, which is defined as the number of electrons injected into the CO molecule normalized by the value at resonant excitation without cavity, is plotted in Fig. 3.4b. The black markers represent the electron injection without a cavity, i.e. the situation in Paper II. The black circle represents resonant excitation (pulse frequency equal to LSP frequency of 3.8 eV). It is placed at the frequency of the LSP resonance along the horizontal axis, and the reference value 1 on the vertical axis. The black triangle connected by a line to the black circle, represents the best enhancement achieved using an off-resonant pulse, the position on the horizontal axis (3.6 eV) represents the frequency used, and the value on the vertical axis the enhancement, which is 1.3. The solid line is a hypothetical enhancement calculated from the data without a cavity, by scaling each off-resonant value so that the energy absorbed is the same as for the resonant case. Each golden circle represents the result using a different cavity volume. The position of the circle along the horizontal axis marks the LP frequency for that particular cavity volume, and the position on the vertical axis the enhancement in electron injection at resonant excitation. The triangles correspond to a more optimal off-resonant excitation. It is interesting to see how the resonantly excited systems in cavities fall closely to the hypothetical efficiency, at least for LP resonances of 3.2 eV and higher. This suggests that the cavity and different frequency of the mode does not fundamentally change the coupling of the LSP, i.e. M_{ia} in Eq. (2.35), to the HCs. Of out all cavity values considered, the maximum enhancement is 6.8 and occurs at 3.0 and 3.2 eV, suggesting that resonance tuning using SC is promising for boosting the efficiency of HC devices.

3.2.3 Modifying reaction rates through vibrational strong coupling

In the concluding section of this chapter, I turn to vibrational SC. This field has emerged after experimental realizations of inhibition [71–73], steering [74], and catalysis [75] of chemical reactions by tuning infrared (IR) cavities to the frequencies of certain vibrational modes of molecules. However, due to the complexity of the nuclear, electronic and cavity degrees of freedom, there are not yet any theoretical studies that successfully describe these processes in agreement with experiment [65]. One framework for vibrational SC simulations was developed in Ref. [76]. This framework numerically propagates forward one idealized cavity coordinate according to Eq. (4.29), the electronic and

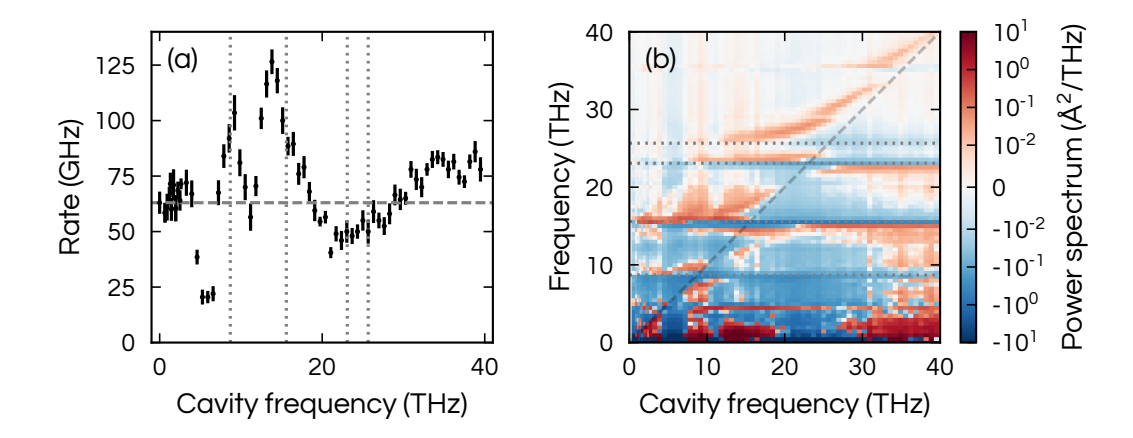


Figure 3.5: (a) Rate of breaking of the Si-C bond under influence of the cavity. Compared to the cavity-free case (Cavity frequency of o, horizontal line), there are both catalyzing and inhibiting frequency regions. (b) Difference in power spectrum of the Si-C bond length compared to the cavity free case. Avoided crossings characteristic of SC are visible near the intersection of the cavity frequency with the important mode frequencies.

nuclear states using RT-TDDFT with Ehrenfest dynamics² with an additional force on the nuclei Eq. (4.34) due to the cavity. Ref. [76] sets up a simulation of the deprotection reaction of 1-phenyl-2-trimethylsilylacetylene (PTA), and captures a resonance dependence of the inhibition of the reaction that is in agreement with experiments [71, 72].

The big drawback of the method in Ref. [76] is its computational cost, and in Paper V, a simplified method based on machine–learned surrogate models is developed. In this model, the potential energy surface (PES) of PTA and a fluoride ion, which initiates the reaction, is obtained from a surrogate model. Likewise, the total (ionic and electronic) dipole moment is obtained from a similar type of model. Without going into the details of the surrogate models, which are described in Paper V, I will state that these models predict values for the energy and dipole moment, given a set of nuclear coordinates, and these values are close to values obtained by density–functional theory (DFT). Then, nuclear and cavity coordinates are propagated forward in time self–consistently, calculating the acceleration on the nuclei from the sum of PES Eq. (4.5) and cavity Eq. (4.34) force, and calculating the cavity coordinate from the dipole moment Eq. (4.29).

Simulations are made for a range of cavity resonance frequencies up to 40 THz (corresponding to 165 meV), with 1000 different initial configurations for each cavity frequency. In Fig. 3.5a, I have plotted the resulting reaction rate of Si–C bond breaking. The rate is strongly dependent on the frequency of the cavity, with an inhibition re-

²In Ehrenfest dynamics the classical limit of nuclei is taken, similar to Eq. (4.5), except that the Born-Oppenheimer approximation is *not* made [77, Chapter 17]. The nuclei are subject to a mean–field potential energy surface (PES) of the excited electronic state.

gion near a cavity frequency of 5 THz, and a catalyzing region near 15 THz. In have also calculated the power spectrum of the Si–C bond length minus its no–cavity value. This quantity (plotted in Fig. 3.5b) illustrates that indeed there are avoided crossings near the intersections of frequencies of certain vibrational modes and the same cavity frequencies. A deeper analysis, that can is provided in Paper V, reveals that the biggest flaw of the model is its missing dependence on the cavity coordinate. This likely makes the model consequently predict too high rates for high cavity frequencies. Yet, the machine–learning framework allows a future extension of the model to include also the dependence on the cavity coordinate.

Computational methods

Matter consists of negatively charged electrons and positively charged atomic nuclei. Electrons are inherently quantum particles. Therefore, it would be wrong to describe the state of an electron in a material by some well—defined position and velocity. Instead, the state has to be defined by a probability distribution or density. On the other hand, the quantum nature of nuclei can often be neglected. In the classical limit, the state of nuclei is described by well—defined positions and velocities evolving in time along some trajectory.

In this chapter, I review the fundamental equations governing the interactions between electrons, nuclei and electromagnetic (EM) radiation on a level appropriate for this thesis. For practical calculations, I introduce the following simplifications. In continuum matter electrodynamics, the electronic and nuclear response is modeled by material specific linear response functions. In density—functional theory (DFT) and time—dependent density—functional theory (TDDFT), an approximate scheme for calculating interactions between electrons, nuclei and EM radiation is provided.

4.1 Fundamental equations

Following Martin [10, Chapter 3], I review the fundamental equations for electrons and nuclei in this section. The starting point is the Born-Oppenheimer approximation [9], which separates the governing equation for electrons and nuclei in two. This approximation works well for the purposes of this thesis [10, Chapter 3], and it is motivated by the different time scales of electronic and nuclear motion, which is related to the large ratio between the mass of nuclei and electrons.

Due to the separation of time scales, the electrons are instantaneously adapted to the positions of nuclei, which are regarded frozen in some geometrical configuration.

Electrons obey the Schrödinger equation

$$H_{\rm BO}\Psi_I = E_I \Psi_I,\tag{4.1}$$

where the Born-Oppenheimer Hamiltonian is

$$H_{\text{BO}} = -\frac{\hbar^2}{2m_e} \sum_{i} \nabla_i^2 + \frac{e^2}{4\pi\epsilon_0} \left(\frac{1}{2} \sum_{i \neq j} \frac{1}{|\mathbf{r}_i - \mathbf{r}_j|} - \sum_{i,I} \frac{Z_I}{|\mathbf{r}_i - \mathbf{R}_I|} + \frac{1}{2} \sum_{I \neq J} \frac{Z_I Z_J}{|\mathbf{R}_I - \mathbf{R}_J|} \right). \tag{4.2}$$

The first term corresponds to the kinetic energy of electrons, and the next three terms to the potential energy of electron–electron, electron–nuclei and nuclei–nuclei interactions. Here, \mathbf{r}_i are positions of electrons, \mathbf{R}_I positions of nuclei, ∇_i the gradient operator in coordinate \mathbf{r}_i , and Z_i the atomic numbers of nuclei. The constants in the equation are the reduced Planck constant \hbar , the electron mass m_e , the vacuum permittivity ε_0 , and the elementary charge e.

The solutions to the Schrödinger equation Eq. (4.1) are a set of eigenstates Ψ_I and eigenenergies E_I . They depend parametrically on the positions of all nuclei R_I through the parametric dependence of the Born-Oppenheimer Hamiltonian Eq. (4.2). The states can be represented in real space by the wave function $\Psi_I(r_1, ..., r_N)$, where $|\Psi_I(r_1, ..., r_N)|^2$ is the probability distribution for the positions of the N electrons. The total energy of the electronic system when the electrons are in an eigenstate I is E_I .

The total energy of the system consists of the energy of the electronic system E_I and the kinetic energy of the nuclei T_n . In the context of nuclear motion, the energy of the electronic system is called the potential energy surface (PES). I will consider the motion of nuclei when the electronic system is in its ground state, and define the ground state PES

$$V_{\text{PES}} = E_0. \tag{4.3}$$

Further taking the classical limit for the nuclei, their kinetic energy is

$$T_{\rm n} = \sum_{I} \frac{1}{2} M_{I} |\dot{R}_{I}|^{2}, \tag{4.4}$$

where M_I and \dot{R}_I are masses and velocities of the nuclei. It can be shown that they follow Newtons laws of motion, with a force on each nucleus

$$F_I = -\nabla_I V_{\text{PFS}},\tag{4.5}$$

where ∇_I is the gradient in the position coordinate of the nuclei R_I .

4.1.1 Interaction of nuclei and electrons with light

Electrons and nuclei also interact with EM radiation, or light. In this thesis, I focus on systems that are much smaller than the wavelengths of interest (which are at least hundreds of nm here). Then, the electric dipole approximation is valid, in which the interaction is mediated through a time-dependent electric field E(t), which is constant over the entire matter system [77, Appendix H]. The Born-Oppenheimer Hamiltonian is rendered time dependent by through the time-dependent electric field:

$$H(t) = H_{BO} - e \left[\sum_{I} Z_{I} \mathbf{R}_{I} - \sum_{i} \mathbf{r}_{i} \right] \cdot E(t). \tag{4.6}$$

Having used the Born-Oppenheimer approximation to separate the timescales of electronic and nuclear motion, it follows that two regimes of frequencies should be treated differently. If the EM field oscillates at near-infrared (IR), visible or ultraviolet (UV) frequencies, then the electronic system is excited, but the nuclei do not react during the short time scales before the system returns to the ground state. The excitations of the electronic system are considered for a frozen configuration of nuclei. The electronic system then obeys the time-dependent Schrödinger equation

$$i\hbar \frac{\partial \Psi_I(t)}{\partial t} = H(t)\Psi_I(t).$$
 (4.7)

If the EM field oscillates at lower IR frequencies, then the electronic system responds instantaneously by being statically polarized by the EM field. The PES, determining the motion of the nuclei, should then be modified to include the polarization of the electronic state

$$\left[H_{\mathrm{BO}} + e \sum_{i} \mathbf{r}_{i} \cdot \mathbf{E}\right] \Psi_{I}(\mathbf{E}) = E_{I}(\mathbf{E}) \Psi_{I}(\mathbf{E}). \tag{4.8}$$

Now the wave functions and energies (including the PES) depend parametrically on the electric field. The force on the nuclei is then

$$F_I(t) = -\nabla_I V_{\text{PES}}(E(t)) + eZ_I E(t), \tag{4.9}$$

The light can be considered external, in the sense that it comes from some accelerating charge distribution far away from the system of interest. But, in principle, the motion of the charged electrons and nuclei also emits EM radiation. Including the back reaction is known as the radiation reaction. In vacuum, this effect is generally negligible [78], but in becomes important in confined environments such as ones described in Sect. 4.2.2.

4.2 Continuum matter electrodynamics

Classical electrodynamics with a continuum description of matter describes the light-matter interaction in terms of susceptibilities of materials: linear functions that tell how the material changes, e.g., its charge distribution in response to an electric field. For practical calculations the susceptibilities can be obtained from other levels of theory, experiment or as simple phenomenological models. In the dipolar limit, retardation effects for the propagation of the EM field are neglected, which simplifies the theory. The review of classical electrodynamics in this section follows Griffiths [79, Chapter 4].

Gauss's law relates the charge distribution in space $\rho(r)$ to the electric field

$$\varepsilon_0 \nabla \cdot E(\mathbf{r}) = \rho(\mathbf{r}). \tag{4.10}$$

The charge distribution is exactly zero in vacuum. In a material, bound charge can be redistributed due to electric fields, as a so-called *bound charge* density

$$\rho(\mathbf{r}) = -\nabla \cdot \mathbf{P}(\mathbf{r}) \tag{4.11}$$

The quantity P(r) is called polarization and is zero in vacuum. Joining the above equations yields (and dropping the explicit (r) from the notation)

$$\nabla \cdot (\varepsilon_0 \mathbf{E} + \mathbf{P}) = 0. \tag{4.12}$$

The term *displacement field* is introduced for $D = \varepsilon_0 E + P$, and the dielectric function (DF) $\varepsilon = (1 + \chi_e)$ is introduced. The latter is a materials property that describes how the material is polarized in response to an electric field. The susceptibility χ_e and DF relate the electric field to the polarization and displacement field

$$P = \varepsilon_0 \gamma_e E \tag{4.13}$$

$$D = \varepsilon_0 \varepsilon E, \tag{4.14}$$

so that Gauss's law can be expressed in the convenient form

$$\nabla \cdot \mathbf{D} = 0. \tag{4.15}$$

To describe time-dependent fields (light), dynamic DFs need to be considered. In principle the DF can be an operator in the form of a convolution over the electric field at all previous times (restricting the discussion to isotropic DFs that are local in space and linear in frequency) [80, Chapter 9]. Hence, a description in the time domain is unnecessarily complicated, and Gauss's law can be expressed in the frequency domain

$$\nabla \cdot \mathbf{D}(\omega) = 0 \tag{4.16}$$

$$D(\omega) = \varepsilon_0 \varepsilon(\omega) E(\omega). \tag{4.17}$$

where the Fourier transform has been introduced¹

$$f(\omega) = \int_{-\infty}^{\infty} f(t)e^{i\omega t} dt.$$
 (4.18)

Here, the dependence of fields on r is implied, and the geometry of materials is encoded in the r-dependence of the DF $\varepsilon(\omega)$. Each Fourier component at frequency ω can be interpreted as a time-dependent field on the form

$$E(t) \sim \text{Re}[E(\omega)e^{-i\omega t}].$$
 (4.19)

The power per area is the irradiance I. In a propagating wave $E(t) = E_0 \sin(\omega t)$ in vacuum it is

$$I = \frac{|E_0|^2}{2} \varepsilon_0 c,\tag{4.20}$$

where *c* is the speed of light.

4.2.1 Dipole expansion of the electric field

For certain charge distributions the electric field has a very simple form. A point charge q at the origin in vacuum has exactly the electric field [79, Chapter 3]

$$E = \frac{q}{4\pi\varepsilon_0} \frac{\mathbf{r}}{r^3},\tag{4.21}$$

¹This definition is used throughout the thesis and the same symbol is used for the variable in the time domain and its Fourier transform.

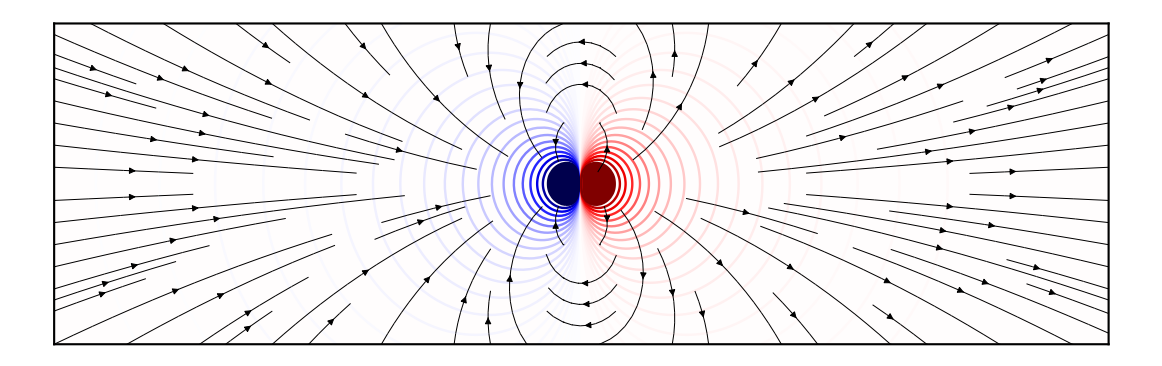


Figure 4.1: Electric field lines and potential isolines for a point dipole.

where r = |r| is the norm of the position vector. For arbitrary charge distributions $\rho(r)$ the expression for the field can be complicated, but can always be expanded in a series in powers of 1/r

$$E = \frac{1}{4\pi\varepsilon_0} \left[\frac{q}{r^3} r + \frac{1}{r^5} \left[3(\mu \cdot r) r - dr^2 \right] + \dots \right],$$
 (4.22)

where the charge q and dipole moment μ are obtained from the charge density

$$q = \int \rho(\mathbf{r}) d\mathbf{r} \tag{4.23}$$

$$\mu = \int \rho(r)r dr. \tag{4.24}$$

The lowest terms in Eq. (4.22) (point charge term $\sim 1/r^2$ and dipole term $\sim 1/r^3$) dominate at large distances from the charge distribution. This turns out to be useful, because far from any localized charge distribution, i.e., any material, the field can be approximated as the field from a charged dipole (Fig. 4.1). The response of the material is characterized by the response of the dipole moment. For a charge neutral material (q=0), the dipole moment is independent of the choice of coordinate system. Using matrix notation for the vectors (\mathbf{r} is a one–column matrix, \mathbf{r}^T its transpose, $\mathbf{r}^T\mathbf{r}'$ an inner product and $\mathbf{r}(\mathbf{r}')^T$ an outer product), the field of a dipole can be written (position and frequency dependence is implied)

$$E_{\text{dipole}} = \frac{1}{4\pi\varepsilon_0} \left[\frac{3rr^{\text{T}}}{r^5} - \frac{1}{r^3} \right] \mu. \tag{4.25}$$

For wavelengths larger than the objects in the system of interest, the field is approximately constant over each object, and it is commonly assume that the following linear relationship holds

$$\mu(\omega) = \alpha(\omega)E(\omega), \tag{4.26}$$

where $\alpha(\omega)$ is the polarizability. The polarizability is in general a tensor of rank two, so that a field in one direction can induce a dipole in another direction. When the response is isotropic, however, $\alpha(\omega)$ can be treated as a scalar. Viewing a small object from a sufficient distance, only the dipole radiation is significant. This leads to an expression for the energy absorbed by the object [81, Chapter 6]. For particles smaller than the wavelength of light, the absorption cross section $C_{\rm abs}$ that relates the irradiance I to the absorbed energy per unit time $W_{\rm abs}$

$$W_{\rm abs} = C_{\rm abs}I,\tag{4.27}$$

where C_{abs} is given by

$$C_{\text{abs}}(\omega) = \frac{2\omega}{c\varepsilon_0} \text{Im } \alpha(\omega).$$
 (4.28)

4.2.2 The single-photonic mode cavity

An idealized Fabry–Perot cavity can be constructed by considering two infinite parallel perfectly conducting planes. Then, only discrete modes of the electric field are allowed, with each mode obeying the equation of motion of a harmonic oscillator. The lowest frequency mode of the cavity is described by the mode coordinate q(t), which is dependent on the history of the nuclear and electronic dipole moment μ through [82, 83]

$$q(t) = \frac{1}{\omega_c} \frac{\boldsymbol{\varepsilon}_c \cdot \boldsymbol{\mu}(0)}{\sqrt{\varepsilon_0 V}} \cos(\omega_c t) + \int_0^t \frac{\boldsymbol{\varepsilon}_c \cdot \boldsymbol{\mu}(t')}{\sqrt{\varepsilon_0 V_c}} \sin(\omega_c (t - t')) dt'$$
(4.29)

Here, ω_c is the frequency of the mode, ε_c the unit vector that describes the polarization of the cavity, and V the effective mode volume of the mode. This form ensures that the mode momentum coordinate is zero $\dot{q}_c(0) = 0$. The field in the center of the cavity is [83]

$$E(t) = \varepsilon_c \left(\frac{\varepsilon_c \cdot \mu(t)}{\varepsilon_0 V} - \frac{q(t)\omega_c}{\sqrt{\varepsilon_0 V}} \right)$$
 (4.30)

The kinetic energy of the cavity is

$$T_c = \frac{1}{2}\dot{q}^2(t) {(4.31)}$$

and the potential energy

$$V_{\text{pot,c}} = \frac{1}{2} \left(\frac{\varepsilon_c \cdot \boldsymbol{\mu}(t)}{\sqrt{\varepsilon_0 V_c}} - q(t) \omega_c \right)^2. \tag{4.32}$$

Then the force from the cavity on nucleus *I* is

$$F_{c,I} = -\nabla_I V_{\text{pot,c}} \tag{4.33}$$

$$= \frac{1}{\sqrt{\varepsilon_0 V_c}} \nabla_I \left[\boldsymbol{\varepsilon}_c \cdot \boldsymbol{\mu} \right] \left(\omega_c q(t) - \frac{\boldsymbol{\varepsilon}_c \cdot \boldsymbol{\mu}(t)}{\sqrt{\varepsilon_0 V_c}} \right) \tag{4.34}$$

4.3 Density functional theory

Unfortunately, the Schrödinger equation is practically not solvable if the material of interest consists of more than a few electrons, because the many–body wave functions Ψ_I are functions of the coordinates of all electrons. Any numerical discretization scheme requires storing and operating on P^{3N} coefficients, P being the number of parameters

per dimension (10 would be an optimistic estimate) and N the number of electrons. Clearly, this is impossible for more than a few electrons, a notion known as the exponential wall [84].

One strategy in electronic structure theory is to reformulate the Schrödinger equation into a form where only the density of electrons

$$\rho_I(\mathbf{r}) = N \int |\Psi_I(\mathbf{r}, \mathbf{r}_2, \dots, \mathbf{r}_N)|^2 d\mathbf{r}_2 \dots d\mathbf{r}_N$$
(4.35)

appears (note that in the previous section ρ denotes *charge* density), and eventually introduce approximations making it computationally tractable. DFT is based on the two Hohenberg–Kohn theorems [85]:

- 1. There is a one-to-one correspondence of the external potential (i.e. from the nuclei) experienced by the electronic system and its ground state electronic density $\rho(\mathbf{r})$.
- 2. There is a universal functional for the total energy of any density $E[\rho]$, exactly equivalent to the Schrödinger equation, and the global minimum of the functional

$$E_{gs} = \min_{\rho(r)} E[\rho] \tag{4.36}$$

is the ground state energy, and the corresponding density the ground state density.

The theorems are valid for densities that can be formed from fermionic wave functions (this property is called N–representability) and that are the ground state density of some external potential (V–representability) [10]. Compared to the Schrödinger equation, the number of numeric coefficients is reduced from P^{3N} to P^{3} which makes DFT more useful for large systems, such as those encountered in materials science. The following section introduces a formalism with an explicit scheme for a density functional $E[\rho]$.

4.3.1 Kohn-Sham density functional theory

Kohn–Sham (KS) DFT [86] provides a tractable scheme for the evaluation of $E[\rho]$ by considering an *auxiliary*, non–explicitly–interacting system of particles instead of the true, explicitly–interacting system of particles. The auxiliary system is governed by the equa-

tions

$$H_{\rm KS}\psi_n = \varepsilon_n \psi_n \tag{4.37}$$

$$H_{\text{KS}} = -\frac{\hbar^2}{2m_e} \nabla^2 + V_{\text{eff}}[\rho](\mathbf{r})$$
 (4.38)

$$\rho(\mathbf{r}) = \sum_{n} f_n \left| \psi_n(\mathbf{r}) \right|^2, \tag{4.39}$$

where f_n is the occupation number of the KS states. In this thesis, I consider spin-paired and non-periodic systems, so I have omitted the degrees of freedom for spin and crystal momentum vectors, which otherwise are needed. In Eq. (4.38) $V_{\rm eff}[\rho](r)$ is an effective potential, and the KS ansatz is that $V_{\rm eff}[\rho](r)$ can be chosen such that the auxiliary system and the true system have the same ground state density. If the assumption holds, which has not formally been proven [10, Chapter 7], it follows from the Hohenberg-Kohn theorems that also the ground state energy of the true system can be obtained from the auxiliary system. The strength of the KS ansatz is that Eq. (4.37) and Eq. (4.38) effectively define a single-particle Schrödinger equation (compare to Eq. (4.1) and Eq. (4.2)) requiring P^3 coefficients to solve. The interactions of electrons are implicitly included through the functional $V_{\rm eff}[\rho](r)$.

An expression for $V_{\rm eff}[\rho](r)$ is obtained by hiding the physics of the interactions in the exchange-correlation (XC) energy functional $E_{\rm xc}[\rho]$, which is formally defined as the difference between the kinetic and electron-electron interaction energies of the true and auxiliary systems [10, Chapter 7]. Its functional derivative is the XC potential functional

$$v_{\rm xc}[\rho](r) = \frac{\delta E_{\rm xc}[\rho]}{\delta \rho}.$$
 (4.40)

Then, the effective potential is comprised of the external potential (i.e. corresponding to the electron–nuclei and nulcei–nuclei interactions in Eq. (4.2)), the Coulomb potential from all electrons in the auxiliary system, and the XC potential that contains everything else [10, Chapter 7]

$$V_{\text{eff}}[\rho](\mathbf{r}) = V_{\text{ext}}(\mathbf{r}) + \frac{e^2}{4\pi\varepsilon_0} \int \frac{\rho(\mathbf{r'})}{|\mathbf{r} - \mathbf{r'}|} d\mathbf{r'} + v_{\text{xc}}[\rho]. \tag{4.41}$$

The total energy functional in KS DFT is [77, Chapter 7]

$$E[\rho] = \sum_{\mathbf{r}} f_{\mathbf{n}} \varepsilon_{\mathbf{n}} - \frac{1}{2} \int \frac{e^2}{4\pi\varepsilon_0} \frac{\rho(\mathbf{r})\rho(\mathbf{r'})}{|\mathbf{r} - \mathbf{r'}|} d\mathbf{r'} d\mathbf{r} + E_{xc}[\rho] - \int v_{xc}[\rho](\mathbf{r})\rho(\mathbf{r}) d\mathbf{r}.$$
(4.42)

For practical calculations, the XC energy and potential functionals have to be approximated, which I discuss in the next section. Self-consistent solutions to Eqs. (4.37)–(4.42) can be found numerically, given functional forms for the XC functional for the

energy, potential, and other observables of interest. Assuming that the KS ansatz is valid and that the exact XC functional is available, this scheme is exactly equivalent to the Schrödinger equation.

4.3.2 The exchange-correlation functional

With an approximate form for the XC functional, electronic structure calculations can readily be carried out. The simplest form is the local density approximation (LDA) [87–89], which is a *local* form for the XC functional, meaning that the value of the potential at every point r depends only on the density at that point. The actual form of the potential is defined to be the same as for a homogeneous electron gas of density n, where the exchange has an exact analytic expression [87, 88], and the correlation is fitted to quantum Monte Carlo calculations [89].

Generalized-gradient approximation (GGA) functionals extend the LDA to depend also on gradients of the density. There are a few different choices for the parametrization of the functional form, that satisfy different exact conditions in limiting cases [10, Chapter 8]. The Perdew-Burke-Ernzerhof (PBE) [90] functional is one such example.

Meta-GGAs try to improve on GGAs by introducing a dependence on the wave functions. The Gritsenko-van Leeuwen-van Lenthe-Baerends (GLLB) [91] functional belongs to this class, and incorporates a discontinuity in the XC potential at integer occupation numbers

$$\Delta_{\mathrm{XC}} = \lim_{\delta \to 0} v_{\mathrm{XC}}(\mathbf{r}, N + \delta) - v_{\mathrm{XC}}(\mathbf{r}, N - \delta) \neq 0 \tag{4.43}$$

which should be a feature of the true XC functional [92]. The GLLB-sc functional [93] is a modification of GLLB with better description of solids and correlation. It greatly improves the location of the d-band in noble metals, which is important for plasmonic systems composed of these metals [25, 94, 95].

Another meta–GGA is the Hubbard +U correction [96], which is added on top of another XC functional in order to change the degree of localization of orbitals. In the form by Dudarev et al. [97] the correction reads

$$E_{+U} = \frac{U}{2} \sum_{a} \text{Tr} \left[\rho^{a} (1 - \rho^{a}) \right], \tag{4.44}$$

where U is a parameter and ρ^a an atomic occupation matrix. It is defined such that positive values of the parameter U penalize partial localization of the KS orbitals. Generally, the sum over atoms a is restricted to atoms of a certain species, and the atomic occupation matrix chosen to include only states of a certain symmetry (often d, in transition metals) [10, Chapter 8]. Then the parameter U is chosen for that species in order to reproduce some experimental or higher–level theory result.

In practice to perform DFT and TDDFT calculations, I use the GPAW code [25, 27, 93, 98–100], relying on the Atomic Simulation Environment [101]. I use the GLLB-sc XC functional for most calculations involving Ag. For calculations where Ag is compared to transition metals, like in Paper I, I instead use PBE with +U corrections. I use the PBE XC functional for calculations without any noble metals.

4.4 Time-dependent density functional theory

Optical absorption and hot carrier (HC) generation processes are not properties of the ground state density, and thus outside of the scope of DFT. However, TDDFT, which appears analogous to DFT, covers these excited state properties, and is the topic of this section.

When the time-dependent Schrödinger equation is on the form

$$i\hbar \frac{\partial}{\partial t} \Psi(t) = [H_0 + V_1(t)] \Psi(t),$$
 (4.45)

the Runge-Gross theorem [102] formally proves the one-to-one correspondence between the scalar potential $V_1(t)$ and initial condition $\Psi(0)$ to the time-dependent electron density $\rho(\mathbf{r},t)$ (defined analogously to Eq. (4.35)). The Runge-Gross theorem is thus the time-dependent analogue of the Hohenberg-Kohn theorem. The analogy to the Kohn-Sham ansatz is the van Leeuwen theorem [103] that is valid under most reasonable circumstances [77, Chapter 3] and states that there is a time-dependent auxiliary system that gives the exact time-dependent density

$$i\hbar \frac{\partial}{\partial t} \psi_n(t) = [H_{\text{KS}}(t) + V_1(t)] \psi_n(t) \tag{4.46}$$

$$H_{\text{KS}}(t) = -\frac{\hbar^2}{2m_c} \nabla^2 + V_{\text{eff}}[\rho](\mathbf{r}, t)$$
(4.47)

$$V_{\text{eff}}[\rho](\mathbf{r},t) = V_{\text{ext}}(\mathbf{r}) + \frac{e^2}{4\pi\varepsilon_0} \int \frac{\rho(\mathbf{r'},t)}{|\mathbf{r}-\mathbf{r'}|} d\mathbf{r'} + v_{\text{xc}}[\rho](t), \tag{4.48}$$

given some initial conditions on the KS wave functions $\psi_i(r,0)$ and their time derivatives. The time–dependent effective potential Eq. (4.48) is similar to the time–independent potential Eq. (4.41). Its first term is the external potential (which is time–independent since the nuclei are considered frozen) and its second term is the instantaneous Coulomb potential. However, the XC functional in the third term depends on the density at all previous times and the initial condition [77, Chapter 4] (the latter condition is formally relaxed by assuming that the potential is zero before t=0; then the initial condition is that the system is in its ground state). The memory–dependence of the XC functional is a complication that is often neglected. This is known as the adiabatic approximation, which is exact when the external potential varies infinitely slowly (causing the system to

always be in its ground state) [77, Chapter 4]. Then, the XC functional is taken to be the ground state XC functional evaluated at the instantaneous density

$$v_{\rm xc}[\rho](t) = v_{\rm xc}[\rho(t)]. \tag{4.49}$$

Absorption spectra of metallic particles computed using the adiabatic approximation have been shown to be consistent with experimental spectra [104, 105], motivating its use in this thesis.

By comparison to Eq. (4.6), the time-dependent external potential is identified

$$V_1(\mathbf{r},t) = -e \left[\sum_{I} Z_I \mathbf{R}_I \delta(\mathbf{r} - \mathbf{R}_I) - \mathbf{r} \right] \cdot E(t). \tag{4.50}$$

Here, E(t) can be an external field, or, for example, the field of a cavity Eq. (4.30). Given a functional form for the XC functional, Eq. (4.46) and Eq. (4.47) can self-consistently be propagated forward in time numerically. This defines the real-time time-dependent density functional theory (RT-TDDFT) method (as opposed to the Casida TDDFT method [23], which is described in Sect. 4.4.1).

4.4.1 Linear response

In this section, I derive a scheme for the response of the time-dependent KS system under linear response conditions, i.e. when the external perturbation E(t) is sufficiently weak. In this context, it is more convenient to a formulation based on the single-particle density operator, which is equivalent to Eq. (4.46). The single-particle density operator is

$$\rho(t) = \sum_{k} f_k |\psi_k(t)\rangle \langle \psi_k(t)|, \tag{4.51}$$

where f_k is the occupation number². Its time evolution is

$$i\hbar \frac{\partial \rho(t)}{\partial t} = H(t)\rho(t) - \rho(t)H(t).$$
 (4.52)

Equation (4.52) can be solved perturbatively [106], by expanding the operators in power series of the perturbation E(t). Neglecting quadratic and higher order terms, the density operator is

$$\rho = \rho^{(0)} + \delta \rho, \tag{4.53}$$

²For numerical reasons, non-integer occupation numbers between 0 and 2 are often used in DFT.

where $\rho^{(0)}$ is the density operator of the unperturbed orbitals and $\delta\rho$ is linear in the perturbation E(t). Likewise, $\delta H(t)$ is taken to be linear in perturbation. For weak perturbations³ the approximation holds well. Inserting these expressions into Eq. (4.52), and again, neglecting quadratic terms from products such as $\delta H(t)\delta\rho(t)$, yields

$$i\hbar \frac{\partial \delta \rho(t)}{\partial t} = H_0 \delta \rho(t) - \delta \rho(t) H_0 + e \mathbf{E}(t) \cdot \left[\mathbf{r} \rho^{(0)} - \rho^{(0)} \mathbf{r} \right] + \left[\delta H \rho^{(0)} - \rho^{(0)} \delta H \right]. \tag{4.54}$$

It is useful to express Eq. (4.54) in the basis of the unperturbed orbitals (i.e. orbitals $\psi_n^{(0)}$ of the system without the external perturbation), by operating on the equation with $\langle \psi_a^{(0)} \rangle$ from the left and $|\psi_i^{(0)}\rangle$ from the right. To this end, I introduce the relations

$$H^{(0)}|\psi_n^{(0)}\rangle = E_n|\psi_n^{(0)}\rangle$$
 (4.55)

$$\rho^{(0)}|\psi_n^{(0)}\rangle = f_n|\psi_n^{(0)}\rangle,$$
 (4.56)

as well as the definitions of the transition energy $\hbar\omega_{ia}=E_a-E_i$ and the occupation number difference $f_{ia}=f_i-f_a$. The following equation is obtained

$$i\hbar \frac{\partial \delta \rho_{ia}(t)}{\partial t} = \hbar \omega_{ia} \delta \rho_{ia}(t) + f_{ia} \mu_{ia} \cdot E(t) + f_{ia} \delta H_{ia}(t), \tag{4.57}$$

where all operators have been expressed in the same basis

$$\delta \rho_{ia}(t) = \langle \psi_a^{(0)} | \delta \rho(t) | \psi_i^{(0)} \rangle \tag{4.58}$$

$$\boldsymbol{\mu}_{ia} = \langle \psi_a^{(0)} | er | \psi_i^{(0)} \rangle \tag{4.59}$$

$$\delta H_{ia}(t) = \langle \psi_a^{(0)} | \delta H(t) | \psi_i^{(0)} \rangle. \tag{4.60}$$

In the adiabatic approximation δH depends only on the instantaneous density and can be expressed as

$$\delta H_{ia} = \sum_{jb} K_{ia,jb} \delta \rho_{jb}, \tag{4.61}$$

where $K_{ia,jb}$ is a coupling matrix which can be found, e.g., in Ref. [23]. Then, the governing equation is

$$i\hbar \frac{\partial \delta \rho_{ia}(t)}{\partial t} = \hbar \omega_{ia} \delta \rho_{ia}(t) + f_{ia} \mu_{ia} \cdot E(t) + f_{ia} \sum_{jb} K_{ia,jb} \delta \rho_{ia}(t), \tag{4.62}$$

 $^{^3}$ This includes the intensity of sunlight on earth, which is about $1000 \, \mathrm{W/m^2}$ or $6 \times 10^{-12} \, \mathrm{eV/fs/nm^2}$. In a particle of absorption cross section 1 nm², each femtosecond of illumination gives a probability of exciting a few–eV electron hole pair on the order of 10^{-12} .

which is a coupled differential equation for the transitions. Because there are no products of $\delta \rho$ or its derivative, and the perturbation E(t), the differential equation is linear, and the solution of $\delta \rho$ should be proportional to the perturbation.

In the basis of the unperturbed orbitals, the density matrix elements $\delta \rho_{ia}$ can be interpreted as the probability of transition from state i to state a. The transition dipole moment μ_{ia} couples the transitions to the external perturbation, and $K_{ia,jb}$ couples pairs of transitions $i \to a$ and $j \to b$. For states with equal occupation numbers $f_{ia} = 0$, the last two terms of Eq. (4.62) are zero and $\delta \rho_{ia}$ has only a trivial time dependence of $\exp(-i\omega_{ia}t)$. This means that, to first order in the perturbation, transitions only occur between states with different occupation numbers. In the following, it is only necessary to consider pairs of occupied states i (where holes can form) and unoccupied states a (to which electrons can be excited), because the opposite pairs are related by symmetry $\delta \rho_{ia} = \delta \rho_{ai}^*$.

Taking the Fourier transform of Eq. (4.62), one obtains the linear system of equations

$$[\hbar\omega - \hbar\omega_{ia}]\,\delta\rho_{ia}(\omega) = f_{ia}\boldsymbol{\mu}_{ia} \cdot \boldsymbol{E}(\omega) + f_{ia}\sum_{jb}K_{ia,jb}\delta\rho_{ia}(\omega). \tag{4.63}$$

Solving this system of equations defines the Casida method [23, 107].

4.4.2 Efficient response calculation in the linear response regime

Since the time—dependent density contains all the information about the quantum system in TDDFT, then the single—particle density matrix can be used to extract observables. The RT—TDDFT and Casida methods are equivalent when sufficiently weak perturbation are used in RT—TDDFT [25], so this method can be used to probe the linear response of any system. **Paper VI** describes the open source software RHODENT, which is used to process RT—TDDFT results obtained from GPAW in order to obtain observables. RHODENT efficiently loads the density matrix in the time or frequency domain, and transforms it to the desired domain.

The induced dipole moment $\delta \mu$ can be obtained as

$$\delta\mu(t) = -\sum_{ia} \mu_{ia} \delta\rho_{ia}(t) \tag{4.64}$$

$$= -\sum_{i < a} \mu_{ia} \left[\delta \rho_{ia}(t) + \delta \rho_{ai}(t) \right], \tag{4.65}$$

where, in the last line, the sum runs only over indices i > a. Using second-order perturbation theory, it can be shown that the transition probability [15]

$$P_{ia} = \frac{\left|\delta \rho_{ia}(t)\right|^2}{f_{ia}}. (4.66)$$

gives the total number of holes in state *i* and electrons in state *a*

$$P_i^{\text{hole}} = -\sum_a P_{ia}$$
, and $P_a^{\text{electron}} = \sum_i P_{ia}$, (4.67)

where the summations are restricted to $f_i > f_a$.

The linear response of the system can also be exploited to efficiently compute the response to a narrow-bandwidth pulse, using the response to a broad-bandwidth perturbation. The broad-bandwidth perturbation can, for example, be a δ -kick which is constant in the frequency domain. In linear response, the density matrix is related to the perturbation E(t) through through a response function χ_{ia} . The relation in the frequency domain is

$$\delta \rho_{ia}(\omega) = \chi_{ia}(\omega) E(\omega). \tag{4.68}$$

Then, given the response $\delta \rho_{1,ia}(t)$ a broad-band perturbation $E_1(t)$, the response to a narrow-band perturbation $E_2(t)$ is obtained as

$$\delta \rho_{2,ia}(\omega) = \chi_{ia}(\omega) E_2(\omega) \tag{4.69}$$

$$=\frac{\delta\rho_{1,ia}(\omega)}{E_1(\omega)}E_2(\omega). \tag{4.70}$$

Outlook

The aim of this thesis has been to understand and exploit light-matter interaction to help design better materials. In particular, I have studied light-matter coupling in the weak and strong regimes, in the context of hot carrier (HC) generation, optical properties, and chemical reactions.

There are a few connections between the attached papers that should be emphasized here. Papers I and II both address HC transfer but in complementary pathways. In Paper I, HCs generated in a metal nanoparticle (NP) are studied, which is of relevance to indirect transfer. In Paper II, HCs separated by the NP-molecule interface are of interest, which is related to direct transfer. Both these pathways are expected to contribute to plasmonic catalysis, with the difference that in indirect transfer, one of the HCs generated in the NP needs to scatter to the orbitals of the molecule in a sequential step. The methodology in Papers I and II is the same, which is manifestation of the versatility of atomistic first-principles simulations like real-time time-dependent density functional theory (RT-TDDFT).

The connection from Paper II to Paper IV is obvious, since the same process in the same system is considered, but with the addition of an idealized cavity that modifies the optical resonance of the system. Again, I used RT-TDDFT. During the work with Papers I, II and IV I developed methods for efficient calculation of response with RT-TDDFT. These include cheap calculation of HC distributions for many different frequencies of a narrow-band laser, using only one (expensive) underlying RT-TDDFT calculation. This work resulted in the RHODENT software, which is accompanied by Paper VI.

Since the optical resonance is shown to be an important handle for controlling HC generation in the Ag-CO system, the computationally efficient method of dipolar coupling (DC) from Paper III is relevant. In fact, a setup considered in Paper IV that I have not shown in this thesis, consists of two identical NPs separated by a small distance (without an idealized cavity), where the molecule approaches one of the NPs. The dis-

tance then controls the resonance, and in order to find suitable geometries for this setup, I used the method of Paper III to quickly estimate the response of the coupled system.

Paper V is the only paper that includes the motion of nuclei. Similar to Paper IV, it also includes an idealized cavity. The simulations in Paper V are computationally tractable, because the potential energy surface (PES) and molecular dipole are precomputed for many atomic configurations and stored in machine learned surrogate models. Then, the simulations are performed with a time resolution that is too coarse to capture the motion of electrons.

A possible extension to the methods of Papers I, II and IV would be to also include nuclear motion in order to model electron—phonon scattering and the long time scale of HC thermalization. Likewise, an implementation of nonadiabatic exchange—correlation (XC) functionals [108, 109] provides a way to model electron—electron scattering in RT—TDDFT; the implementation of such a functional would enable the study of realistic electron scattering and the short time scales of HC thermalization. The inclusion of these two effects would lead to more accurate HC distributions.

Many plasmonic catalysis experiments are done in reaction chambers where reaction products are measured using chromatography [40, 47, 110–112], or photocurrents from the collection of HCs are measured [36, 113]. Developing a tractable complete theoretical model for the photocatalysis of a chemical reaction, that takes into account intricacies associated with atomic structure of the materials, is tremendously challenging. Surface hopping [114] has been used in Ref. [115] to model electron–phonon scattering and nuclear motion, and would be suitable to capture both the HC thermalization and chemical kinetics.

Another possible direction of future work is the extension of the DC method to higher-order multipoles, which should improve accuracy for NPs at short separations where near-field gradients are strong. Once the coupled response is captured with sufficient fidelity, one can pursue a mixed quantum—classical strategy: treat the chemically active region (e.g., NP and molecule) quantum mechanically to resolve HCs, while representing the system(s) in the environment classically, with the two (or more) subsystems exchanging fields self—consistently via electrodynamics. This "electrodynamic embedding" would make simulations of very large assemblies computationally tractable, for example to study realistic disordered systems, or ensembles of systems in collective strong coupling (SC). Its main limitation is the absence of explicit hybridization across the quantum—classical boundary, which sets a lower bound on realistic gap sizes.

Similar ideas of quantum-classical separation have been explored in the literature. In Ref. [83], a framework has been derived for coupling of a RT-TDDFT subsystem to any electromagnetic (EM) structure (as opposed to an idealized cavity) through a dyadic Greens tensor that can be obtained with standard EM solvers. Another, slightly different idea has been implemented in Ref. [116], where the spatially and temporally resolved electric potential has been calculated in a two-NP system using quasi-electrostatics, and HCs calculated quantum mechanically using the precalculated potential.

Acknowledgments

First I wish to thank Paul Erhart, my main supervisor, for your belief in me. You have given me quite free reins in shaping my PhD thesis, which has allowed me to develop confidence in my abilities. You have always spurred me to learn new topics, present my findings in a better way, and write better code. I don't know how I would have learned so much about condensed matter, code quality, writing, presenting, and typesetting, under the supervision of anyone else. I am also grateful to my assistant supervisors, Tuomas Rossi and Christian Schäfer. Thank you Tuomas for your patience with big and small questions, and for the time you have invested in teaching me about TDDFT and the inner workings of GPAW. You have set the standard for how code review is done, and I will take this with me. Thank you Christian for always being there to answer my questions. I don't think I ever had a question about TDDFT, or any other theory, that you were not able to answer. Thank you all for your help with discussing, proof reading, and editing my papers and thesis.

I also want to thank all the past and present members of the CMM division for making the workplace a fun and stimulating environment. I can always count on finding someone to discuss anything from food to music to the best trails for cross country running in Göteborg.

Finally, I am grateful for my friends and family for being there, and shaping me as a person. I want to thank my parents for encouraging my physics and programming interests and encouraging my higher education. And at last, thank you to my wife Isabel, who has been patient and loving to me and provided unfailing support. It is the best moment of every day to come home to you and our son Casper.

Bibliography

- [1] A. Polman, M. Knight, E. C. Garnett, B. Ehrler, and W. C. Sinke, *Photovoltaic Materials: Present Efficiencies and Future Challenges*, Science **352**, aad4424 (2016). doi:10.1126/science. aad4424.
- [2] J. Yang, D. Wang, H. Han, and C. Li, Roles of Cocatalysts in Photocatalysis and Photoelectrocatalysis, Accounts of Chemical Research 46, 1900 (2013). doi:10.1021/ar300227e.
- [3] E. Cortés, L. V. Besteiro, A. Alabastri, A. Baldi, G. Tagliabue, A. Demetriadou, and P. Narang, *Challenges in Plasmonic Catalysis*, ACS Nano 14, 16202 (2020). doi:10.1021/acsnano.0c08773.
- [4] F. A. A. Nugroho, I. Darmadi, L. Cusinato, A. Susarrey-Arce, H. Schreuders, L. J. Bannenberg, A. B. da Silva Fanta, S. Kadkhodazadeh, J. B. Wagner, T. J. Antosiewicz, A. Hellman, V. P. Zhdanov, B. Dam, and C. Langhammer, *Metal-Polymer Hybrid Nanomaterials for Plasmonic Ultrafast Hydrogen Detection*, Nature Materials 18, 489 (2019). doi:10.1038/s41563-019-0325-4.
- [5] C. Bie, L. Wang, and J. Yu, Challenges for Photocatalytic Overall Water Splitting, Chem 8, 1567 (2022). doi:10.1016/j.chempr.2022.04.013.
- [6] IPCC, Summary for Policymakers, in Climate Change 2022: Mitigation of Climate Change. Contribution of Working Group III to the Sixth Assessment Report of the Intergovernmental Panel on Climate Change, edited by P. Shukla, J. Skea, R. Slade, A. A. Khourdajie, R. van Diemen, D. McCollum, M. Pathak, S. Some, P. Vyas, R. Fradera, M. Belkacemi, A. Hasija, G. Lisboa, S. Luz, and J. Malley (Cambridge, UK and New York, NY, USA: Cambridge University Press, 2022), p. 3. doi:10.1017/9781009157926.001.
- [7] T. W. Ebbesen, *Hybrid Light–Matter States in a Molecular and Material Science Perspective*, Accounts of Chemical Research **49**, 2403 (2016). doi:10.1021/acs.accounts.6b00295.
- [8] A. P. Sutton, *Electronic Structure of Materials* (Oxford : New York: Clarendon Press ; Oxford University Press, 1993). ISBN 978-0-19-851755-9 978-0-19-851754-2.
- [9] M. Born and R. Oppenheimer, *Zur Quantentheorie Der Molekeln*, Annalen der Physik **389**, 457 (1927). doi:10.1002/andp.19273892002.
- [10] R. M. Martin, Electronic Structure: Basic Theory and Practical Methods (Cambridge University Press, 2004). ISBN 978-0-521-53440-6 978-0-521-78285-2 978-0-511-80576-9. doi: 10.1017/CBO9780511805769.
- [11] D. J. Griffiths, Introduction to Quantum Mechanics (Englewood Cliffs, N.J: Prentice Hall, 1995). ISBN 978-0-13-124405-4.

- [12] C. F. Bohren, How Can a Particle Absorb More than the Light Incident on It?, American Journal of Physics **51**, 323 (1983). doi:10.1119/1.13262.
- [13] M. L. Brongersma, N. J. Halas, and P. Nordlander, *Plasmon-Induced Hot Carrier Science and Technology*, Nature Nanotechnology **10**, 25 (2015). doi:10.1038/nnano.2014.311.
- [14] P. V. Kumar, T. P. Rossi, D. Marti-Dafcik, D. Reichmuth, M. Kuisma, P. Erhart, M. J. Puska, and D. J. Norris, *Plasmon-Induced Direct Hot-Carrier Transfer at Metal–Acceptor Interfaces*, ACS Nano 13, 3188 (2019). doi:10.1021/acsnano.8b08703.
- [15] T. P. Rossi, P. Erhart, and M. Kuisma, *Hot-Carrier Generation in Plasmonic Nanoparticles: The Importance of Atomic Structure*, ACS Nano 14, 9963 (2020). doi:10.1021/acsnano.0c03004.
- [16] J. Ma and S. Gao, Plasmon-Induced Electron–Hole Separation at the Ag/TiO_2 (110) Interface, ACS Nano 13, 13658 (2019). doi:10.1021/acsnano.9b03555.
- [17] P. B. Johnson and R. W. Christy, *Optical Constants of the Noble Metals*, Physical Review B **6**, 4370 (1972). doi:10.1103/PhysRevB.6.4370.
- [18] G. Mie, Beiträge Zur Optik Trüber Medien, Speziell Kolloidaler Metallösungen, Annalen der Physik 330, 377 (1908). doi:10.1002/andp.19083300302.
- [19] K. Ladutenko, U. Pal, A. Rivera, and O. Peña-Rodríguez, Mie Calculation of Electromagnetic Near-Field for a Multilayered Sphere, Computer Physics Communications **214**, 225 (2017). doi: 10.1016/j.cpc.2017.01.017.
- [20] A. Sihvola, *Dielectric Polarization and Particle Shape Effects*, Journal of Nanomaterials **2007**, 1 (2007). doi:10.1155/2007/45090.
- [21] M. A. Cazalilla, J. S. Dolado, A. Rubio, and P. M. Echenique, *Plasmonic Excitations in Noble Metals: The Case of Ag*, Physical Review B **61**, 8033 (2000). doi:10.1103/PhysRevB.61. 8033.
- [22] M. Rahm, There Is an Alloy at the End of the Rainbow: Structure and Optical Properties From Bulk to Nano. PhD thesis, Chalmers University of Technology, 2021.
- [23] M. E. Casida, Time-Dependent Density Functional Response Theory for Molecules. In , Recent Advances in Computational Chemistry (WORLD SCIENTIFIC, 1995). doi:10.1142/9789812830586_0005.
- [24] S. Malola, L. Lehtovaara, J. Enkovaara, and H. Häkkinen, Birth of the Localized Surface Plasmon Resonance in Monolayer-Protected Gold Nanoclusters, ACS Nano 7, 10263 (2013). doi: 10.1021/nn4046634.
- [25] M. Kuisma, A. Sakko, T. P. Rossi, A. H. Larsen, J. Enkovaara, L. Lehtovaara, and T. T. Rantala, Localized Surface Plasmon Resonance in Silver Nanoparticles: Atomistic First-Principles Time-Dependent Density-Functional Theory Calculations, Physical Review B 91, 115431 (2015). doi:10.1103/PhysRevB.91.115431.
- [26] S. Raza, W. Yan, N. Stenger, M. Wubs, and N. A. Mortensen, Blueshift of the Surface Plasmon Resonance in Silver Nanoparticles: Substrate Effects, Optics Express 21, 27344 (2013). doi:10. 1364/OE.21.027344.
- [27] T. P. Rossi, M. Kuisma, M. J. Puska, R. M. Nieminen, and P. Erhart, Kohn-Sham Decomposition in Real-Time Time-Dependent Density-Functional Theory: An Efficient Tool for Analyzing Plasmonic Excitations, Journal of Chemical Theory and Computation 13, 4779 (2017). doi:10.1021/acs.jctc.7b00589.

- [28] M. Bernardi, J. Mustafa, J. B. Neaton, and S. G. Louie, *Theory and Computation of Hot Carriers Generated by Surface Plasmon Polaritons in Noble Metals*, Nature Communications **6**, 7044 (2015). doi:10.1038/ncomms8044.
- [29] H. Jin, J. M. Kahk, D. A. Papaconstantopoulos, A. Ferreira, and J. Lischner, *Plasmon-Induced Hot Carriers from Interband and Intraband Transitions in Large Noble Metal Nanoparticles*, PRX Energy 1, 013006 (2022). doi:10.1103/PRXEnergy.1.013006.
- [30] S. Ramachandran, S. M. João, H. Jin, and J. Lischner, *Hot Carriers from Intra- and Interband Transitions in Gold-Silver Alloy Nanoparticles*, Communications Chemistry **7**, 169 (2024). doi: 10.1038/s42004-024-01244-w.
- [31] R. Sundararaman, P. Narang, A. S. Jermyn, W. A. Goddard III, and H. A. Atwater, *Theoretical Predictions for Hot-Carrier Generation from Surface Plasmon Decay*, Nature Communications **5**, 5788 (2014). doi:10.1038/ncomms6788.
- [32] L. Wittenbecher, E. Viñas Boström, J. Vogelsang, S. Lehman, K. A. Dick, C. Verdozzi, D. Zigmantas, and A. Mikkelsen, *Unraveling the Ultrafast Hot Electron Dynamics in Semiconductor Nanowires*, ACS Nano 15, 1133 (2021). doi:10.1021/acsnano.0c08101.
- [33] R. E. Bangle and M. H. Mikkelsen, *Tracking Light-Induced Charge Transport*, Science **382**, 264 (2023). doi:10.1126/science.adk6862.
- [34] Y. Zhu, M. B. Raschke, D. Natelson, and L. Cui, Molecular Scale Nanophotonics: Hot Carriers, Strong Coupling, and Electrically Driven Plasmonic Processes, Nanophotonics 13, 2281 (2024). doi:10.1515/nanoph-2023-0710.
- [35] X. Geng, M. Abdellah, R. Bericat Vadell, M. Folkenant, T. Edvinsson, and J. Sá, Direct Plasmonic Solar Cell Efficiency Dependence on Spiro-OMeTAD Li-TFSI Content, Nanomaterials 11, 3329 (2021). doi:10.3390/nano11123329.
- [36] J. S. DuChene, G. Tagliabue, A. J. Welch, W.-H. Cheng, and H. A. Atwater, *Hot Hole Collection and Photoelectrochemical CO2 Reduction with Plasmonic Au/p-GaN Photocathodes*, Nano Letters 18, 2545 (2018). doi:10.1021/acs.nanolett.8b00241.
- [37] G. Tagliabue, J. S. DuChene, M. Abdellah, A. Habib, D. J. Gosztola, Y. Hattori, W.-H. Cheng, K. Zheng, S. E. Canton, R. Sundararaman, J. Sá, and H. A. Atwater, *Ultrafast Hot-Hole Injection Modifies Hot-Electron Dynamics in Au/p-GaN Heterostructures*, Nature Materials 19, 1312 (2020). doi:10.1038/s41563-020-0737-1.
- [38] R. Li, W.-H. Cheng, M. H. Richter, J. S. DuChene, W. Tian, C. Li, and H. A. Atwater, Unassisted Highly Selective Gas-Phase CO2 Reduction with a Plasmonic Au/p-GaN Photocatalyst Using H2O as an Electron Donor, ACS Energy Letters 6, 1849 (2021). doi:10.1021/acsenergylett. 1c00392.
- [39] P. Christopher, H. Xin, and S. Linic, Visible-Light-Enhanced Catalytic Oxidation Reactions on Plasmonic Silver Nanostructures, Nature Chemistry 3, 467 (2011). doi:10.1038/nchem. 1032.
- [40] U. Aslam, S. Chavez, and S. Linic, Controlling Energy Flow in Multimetallic Nanostructures for Plasmonic Catalysis, Nature Nanotechnology 12, 1000 (2017). doi:10.1038/nnano.2017. 131.

- [41] U. Aslam, V. G. Rao, S. Chavez, and S. Linic, Catalytic Conversion of Solar to Chemical Energy on Plasmonic Metal Nanostructures, Nature Catalysis 1, 656 (2018). doi:10.1038/s41929-018-0138-x.
- [42] L. Zhou, M. Lou, J. L. Bao, C. Zhang, J. G. Liu, J. M. P. Martirez, S. Tian, L. Yuan, D. F. Swearer, H. Robatjazi, E. A. Carter, P. Nordlander, and N. J. Halas, *Hot Carrier Multiplication in Plasmonic Photocatalysis*, Proceedings of the National Academy of Sciences 118, e2022109118 (2021). doi:10.1073/pnas.2022109118.
- [43] T. Hou, L. Chen, Y. Xin, W. Zhu, C. Zhang, W. Zhang, S. Liang, and L. Wang, *Porous CuFe for Plasmon-Assisted N2 Photofixation*, ACS Energy Letters **5**, 2444 (2020). doi:10.1021/acsenergylett.0c00959.
- [44] Y. Yamazaki, Y. Kuwahara, K. Mori, T. Kamegawa, and H. Yamashita, *Enhanced Catalysis of Plasmonic Silver Nanoparticles by a Combination of Macro-/Mesoporous Nanostructured Silica Support*, The Journal of Physical Chemistry C **125**, 9150 (2021). doi:10.1021/acs.jpcc. 1c01669.
- [45] H. Ren, J.-L. Yang, W.-M. Yang, H.-L. Zhong, J.-S. Lin, P. M. Radjenovic, L. Sun, H. Zhang, J. Xu, Z.-Q. Tian, and J.-F. Li, Core-Shell-Satellite Plasmonic Photocatalyst for Broad-Spectrum Photocatalytic Water Splitting, ACS Materials Letters 3, 69 (2021). doi:10. 1021/acsmaterialslett.0c00479.
- [46] S. Linic, U. Aslam, C. Boerigter, and M. Morabito, *Photochemical Transformations on Plasmonic Metal Nanoparticles*, Nature Materials **14**, 567 (2015). doi:10.1038/nmat4281.
- [47] S. Mukherjee, F. Libisch, N. Large, O. Neumann, L. V. Brown, J. Cheng, J. B. Lassiter, E. A. Carter, P. Nordlander, and N. J. Halas, *Hot Electrons Do the Impossible: Plasmon-Induced Dissociation of H2 on Au*, Nano Letters 13, 240 (2013). doi:10.1021/nl303940z.
- [48] B. Seemala, A. J. Therrien, M. Lou, K. Li, J. P. Finzel, J. Qi, P. Nordlander, and P. Christopher, *Plasmon-Mediated Catalytic O2 Dissociation on Ag Nanostructures: Hot Electrons or Near Fields?*, ACS Energy Letters 4, 1803 (2019). doi:10.1021/acsenergylett.9b00990.
- [49] S.-C. Huang, X. Wang, Q.-Q. Zhao, J.-F. Zhu, C.-W. Li, Y.-H. He, S. Hu, M. M. Sartin, S. Yan, and B. Ren, *Probing Nanoscale Spatial Distribution of Plasmonically Excited Hot Carriers*, Nature Communications 11, 4211 (2020). doi:10.1038/s41467-020-18016-4.
- [50] J. B. Khurgin, A. Petrov, M. Eich, and A. V. Uskov, Direct Plasmonic Excitation of the Hybridized Surface States in Metal Nanoparticles, ACS Photonics 8, 2041 (2021). doi:10.1021/acsphotonics.1c00167.
- [51] P. V. Kumar, T. P. Rossi, M. Kuisma, P. Erhart, and D. J. Norris, *Direct Hot-Carrier Transfer in Plasmonic Catalysis*, Faraday Discussions **214**, 189 (2019). doi:10.1039/C8FD00154E.
- [52] L. Ranno, S. Dal Forno, and J. Lischner, Computational Design of Bimetallic Core-Shell Nanoparticles for Hot-Carrier Photocatalysis, npj Computational Materials 4, 31 (2018). doi: 10.1038/s41524-018-0088-5.
- [53] J. M. Rahm, C. Tiburski, T. P. Rossi, F. A. A. Nugroho, S. Nilsson, C. Langhammer, and P. Erhart, A Library of Late Transition Metal Alloy Dielectric Functions for Nanophotonic Applications, Advanced Functional Materials 30, 2002122 (2020). doi:10.1002/adfm. 202002122.

- [54] C. Tiburski and C. Langhammer, Engineering Optical Absorption in Late Transition-Metal Nanoparticles by Alloying, ACS Photonics 10, 253 (2023). doi:10.1021/acsphotonics. 2c01597.
- [55] J. Li, S. K. Cushing, J. Bright, F. Meng, T. R. Senty, P. Zheng, A. D. Bristow, and N. Wu, Ag@Cu2O Core-Shell Nanoparticles as Visible-Light Plasmonic Photocatalysts, ACS Catalysis 3, 47 (2013). doi:10.1021/cs300672f.
- [56] D. F. Swearer, H. Zhao, L. Zhou, C. Zhang, H. Robatjazi, J. M. P. Martirez, C. M. Krauter, S. Yazdi, M. J. McClain, E. Ringe, E. A. Carter, P. Nordlander, and N. J. Halas, *Heterometallic Antenna-reactor Complexes for Photocatalysis*, Proceedings of the National Academy of Sciences 113, 8916 (2016). doi:10.1073/pnas.1609769113.
- [57] L. Zhou, J. M. P. Martirez, J. Finzel, C. Zhang, D. F. Swearer, S. Tian, H. Robatjazi, M. Lou, L. Dong, L. Henderson, P. Christopher, E. A. Carter, P. Nordlander, and N. J. Halas, *Light-Driven Methane Dry Reforming with Single Atomic Site Antenna-Reactor Plasmonic Photocatalysts*, Nature Energy 5, 61 (2020). doi:10.1038/s41560-019-0517-9.
- [58] L. Román Castellanos, O. Hess, and J. Lischner, Dielectric Engineering of Hot-Carrier Generation by Quantized Plasmons in Embedded Silver Nanoparticles, The Journal of Physical Chemistry C 125, 3081 (2021). doi:10.1021/acs.jpcc.0c07617.
- [59] X. Wu, S. K. Gray, and M. Pelton, Quantum-Dot-Induced Transparency in a Nanoscale Plasmonic Resonator, Optics Express 18, 23633 (2010). doi:10.1364/OE.18.023633.
- [60] T. Schwartz, J. A. Hutchison, J. Léonard, C. Genet, S. Haacke, and T. W. Ebbesen, *Polariton Dynamics under Strong Light–Molecule Coupling*, ChemPhysChem **14**, 125 (2013). doi: 10.1002/cphc.201200734.
- [61] C. Zhang, H. Hu, C. Ma, Y. Li, X. Wang, D. Li, A. Movsesyan, Z. Wang, A. Govorov, Q. Gan, and T. Ding, Quantum Plasmonics Pushes Chiral Sensing Limit to Single Molecules: A Paradigm for Chiral Biodetections, Nature Communications 15, 2 (2024). doi:10.1038/s41467-023-42719-z.
- [62] K. Nagarajan, A. Thomas, and T. W. Ebbesen, *Chemistry under Vibrational Strong Coupling*, Journal of the American Chemical Society **143**, 16877 (2021). doi:10.1021/jacs.1c07420.
- [63] L. P. Lindoy, A. Mandal, and D. R. Reichman, Quantum Dynamical Effects of Vibrational Strong Coupling in Chemical Reactivity, Nature Communications 14, 2733 (2023). doi:10. 1038/s41467-023-38368-x.
- [64] D. Sidler, T. Schnappinger, A. Obzhirov, M. Ruggenthaler, M. Kowalewski, and A. Rubio, *Unraveling a Cavity-Induced Molecular Polarization Mechanism from Collective Vibrational Strong Coupling*, The Journal of Physical Chemistry Letters **15**, 5208 (2024). doi:10.1021/acs.jpclett.4c00913.
- [65] F. J. Garcia-Vidal, C. Ciuti, and T. W. Ebbesen, *Manipulating Matter by Strong Coupling to Vacuum Fields*, Science **373**, eabdo336 (2021). doi:10.1126/science.abd0336.
- [66] P. Törmä and W. L. Barnes, Strong Coupling between Surface Plasmon Polaritons and Emitters: A Review, Reports on Progress in Physics **78**, 013901 (2014). doi:10.1088/0034-4885/78/1/013901.

- [67] E. Jaynes and F. Cummings, Comparison of Quantum and Semiclassical Radiation Theories with Application to the Beam Maser, Proceedings of the IEEE **51**, 89 (1963). doi:10.1109/PROC. 1963.1664.
- [68] T. P. Rossi, T. Shegai, P. Erhart, and T. J. Antosiewicz, *Strong Plasmon-Molecule Coupling at the Nanoscale Revealed by First-Principles Modeling*, Nature Communications **10**, 3336 (2019). doi:10.1038/s41467-019-11315-5.
- [69] M. Kaniber, K. Schraml, A. Regler, J. Bartl, G. Glashagen, F. Flassig, J. Wierzbowski, and J. J. Finley, Surface Plasmon Resonance Spectroscopy of Single Bowtie Nano-Antennas Using a Differential Reflectivity Method, Scientific Reports 6, 23203 (2016). doi:10.1038/srep23203.
- [70] J. J. Baumberg, J. Aizpurua, M. H. Mikkelsen, and D. R. Smith, Extreme Nanophotonics from Ultrathin Metallic Gaps, Nature Materials 18, 668 (2019). doi:10.1038/s41563-019-0290-y.
- [71] A. Thomas, J. George, A. Shalabney, M. Dryzhakov, S. J. Varma, J. Moran, T. Chervy, X. Zhong, E. Devaux, C. Genet, J. A. Hutchison, and T. W. Ebbesen, *Ground-State Chemical Reactivity under Vibrational Coupling to the Vacuum Electromagnetic Field*, Angewandte Chemie International Edition 55, 11462 (2016). doi:10.1002/anie.201605504.
- [72] A. Thomas, A. Jayachandran, L. Lethuillier-Karl, R. M. A. Vergauwe, K. Nagarajan, E. Devaux, C. Genet, J. Moran, and T. W. Ebbesen, *Ground State Chemistry under Vibrational Strong Coupling: Dependence of Thermodynamic Parameters on the Rabi Splitting Energy*, Nanophotonics 9, 249 (2020). doi:10.1515/nanoph-2019-0340.
- [73] W. Ahn, J. F. Triana, F. Recabal, F. Herrera, and B. S. Simpkins, Modification of Ground-State Chemical Reactivity via Light-Matter Coherence in Infrared Cavities, Science 380, 1165 (2023). doi:10.1126/science.ade7147.
- [74] A. Thomas, L. Lethuillier-Karl, K. Nagarajan, R. M. A. Vergauwe, J. George, T. Chervy, A. Shalabney, E. Devaux, C. Genet, J. Moran, and T. W. Ebbesen, *Tilting a Ground-State Reactivity Landscape by Vibrational Strong Coupling*, Science **363**, 615 (2019). doi:10.1126/science.aau7742.
- [75] J. Lather, P. Bhatt, A. Thomas, T. W. Ebbesen, and J. George, *Cavity Catalysis by Cooperative Vibrational Strong Coupling of Reactant and Solvent Molecules*, Angewandte Chemie International Edition **58**, 10635 (2019). doi:10.1002/anie.201905407.
- [76] C. Schäfer, J. Flick, E. Ronca, P. Narang, and A. Rubio, Shining Light on the Microscopic Resonant Mechanism Responsible for Cavity-Mediated Chemical Reactivity, Nature Communications 13, 7817 (2022). doi:10.1038/s41467-022-35363-6.
- [77] C. A. Ullrich, Review of Ground-State Density-Functional Theory, in Time-Dependent Density-Functional Theory (Oxford University Press, 2011), p. 10.
- [78] J. D. Jackson, Classical Electrodynamics (New York: Wiley, 1962). ISBN 978-0-471-43131-2.
- [79] D. J. Griffiths, Introduction to Electrodynamics (Upper Saddle River, NJ: Pearson, 1998).
- [80] L. D. Landau, E. M. Lifshitz, and L. P. Pitaevskii, *Electrodynamics of Continuous Media* (Oxford, England: Butterworth-Heinemann, 1984).
- [81] H. C. van der Hulst, *Light Scattering by Small Particles* (Mineola, NY: Dover Publications, 1981).

- [82] C. Schäfer, M. Ruggenthaler, and A. Rubio, Ab Initio Nonrelativistic Quantum Electrodynamics: Bridging Quantum Chemistry and Quantum Optics from Weak to Strong Coupling, Physical Review A 98, 043801 (2018). doi:10.1103/PhysRev A.98.043801.
- [83] C. Schäfer and G. Johansson, Shortcut to Self-Consistent Light-Matter Interaction and Realistic Spectra from First Principles, Physical Review Letters 128, 156402 (2022). doi:10.1103/PhysRevLett.128.156402.
- [84] W. Kohn, Nobel Lecture: Electronic Structure of Matter—Wave Functions and Density Functionals, Reviews of Modern Physics 71, 1253 (1999). doi:10.1103/RevModPhys.71.1253.
- [85] P. Hohenberg and W. Kohn, *Inhomogeneous Electron Gas*, Physical Review **136**, B864 (1964). doi:10.1103/PhysRev.136.B864.
- [86] W. Kohn and L. J. Sham, *Self-Consistent Equations Including Exchange and Correlation Effects*, Physical Review **140**, A1133 (1965). doi:10.1103/PhysRev.140.A1133.
- [87] P. A. M. Dirac, Note on Exchange Phenomena in the Thomas Atom, Mathematical Proceedings of the Cambridge Philosophical Society **26**, 376 (1930). doi:10.1017/S0305004100016108.
- [88] F. Bloch, Bemerkung zur Elektronentheorie des Ferromagnetismus und der elektrischen Leitfähigkeit, Zeitschrift für Physik **57**, 545 (1929). doi:10.1007/BF01340281.
- [89] J. P. Perdew and A. Zunger, Self-Interaction Correction to Density-Functional Approximations for Many-Electron Systems, Physical Review B 23, 5048 (1981). doi:10.1103/PhysRevB.23. 5048.
- [90] J. P. Perdew, K. Burke, and M. Ernzerhof, *Generalized Gradient Approximation Made Simple*, Physical Review Letters **77**, 3865 (1996). doi:10.1103/PhysRevLett.77.3865.
- [91] O. Gritsenko, R. van Leeuwen, E. van Lenthe, and E. J. Baerends, Self-Consistent Approximation to the Kohn-Sham Exchange Potential, Physical Review A 51, 1944 (1995). doi:10.1103/PhysRev A.51.1944.
- [92] J. P. Perdew and M. Levy, *Physical Content of the Exact Kohn-Sham Orbital Energies: Band Gaps and Derivative Discontinuities*, Physical Review Letters **51**, 1884 (1983). doi:10.1103/PhysRevLett.51.1884.
- [93] M. Kuisma, J. Ojanen, J. Enkovaara, and T. T. Rantala, *Kohn-Sham Potential with Discontinuity for Band Gap Materials*, Physical Review B **82**, 115106 (2010). doi:10.1103/PhysRevB. 82.115106.
- [94] J. Yan, K. W. Jacobsen, and K. S. Thygesen, First-Principles Study of Surface Plasmons on Ag(111) and H/Ag(111), Physical Review B **84**, 235430 (2011). doi:10.1103/PhysRevB.84.235430.
- [95] J. Yan, K. W. Jacobsen, and K. S. Thygesen, Conventional and Acoustic Surface Plasmons on Noble Metal Surfaces: A Time-Dependent Density Functional Theory Study, Physical Review B 86, 241404 (2012). doi:10.1103/PhysRevB.86.241404.
- [96] A. I. Liechtenstein, V. I. Anisimov, and J. Zaanen, Density-Functional Theory and Strong Interactions: Orbital Ordering in Mott-Hubbard Insulators, Physical Review B **52**, R5467 (1995). doi:10.1103/PhysRevB.52.R5467.
- [97] S. L. Dudarev, G. A. Botton, S. Y. Savrasov, C. J. Humphreys, and A. P. Sutton, *Electron-Energy-Loss Spectra and the Structural Stability of Nickel Oxide: An LSDA+U Study*, Physical Review B **57**, 1505 (1998). doi:10.1103/PhysRevB.57.1505.

- [98] J. J. Mortensen, A. H. Larsen, M. Kuisma, A. V. Ivanov, A. Taghizadeh, A. Peterson, A. Haldar, A. O. Dohn, C. Schäfer, E. Ö. Jónsson, E. D. Hermes, F. A. Nilsson, G. Kastlunger, G. Levi, H. Jónsson, H. Häkkinen, J. Fojt, J. Kangsabanik, J. Sødequist, J. Lehtomäki, J. Heske, J. Enkovaara, K. T. Winther, M. Dulak, M. M. Melander, M. Ovesen, M. Louhivuori, M. Walter, M. Gjerding, O. Lopez-Acevedo, P. Erhart, R. Warmbier, R. Würdemann, S. Kaappa, S. Latini, T. M. Boland, T. Bligaard, T. Skovhus, T. Susi, T. Maxson, T. Rossi, X. Chen, Y. L. A. Schmerwitz, J. Schiøtz, T. Olsen, K. W. Jacobsen, and K. S. Thygesen, *GPAW: An Open Python Package for Electronic Structure Calculations*, The Journal of Chemical Physics 160, 092503 (2024). doi:10.1063/5.0182685.
- [99] J. J. Mortensen, L. B. Hansen, and K. W. Jacobsen, Real-Space Grid Implementation of the Projector Augmented Wave Method, Physical Review B 71, 035109 (2005). doi:10.1103/PhysRevB.71.035109.
- [100] A. H. Larsen, M. Vanin, J. J. Mortensen, K. S. Thygesen, and K. W. Jacobsen, Localized Atomic Basis Set in the Projector Augmented Wave Method, Physical Review B 80, 195112 (2009). doi:10.1103/PhysRevB.80.195112.
- [101] A. H. Larsen, J. J. Mortensen, J. Blomqvist, I. E. Castelli, R. Christensen, M. Dułak, J. Friis, M. N. Groves, B. Hammer, C. Hargus, E. D. Hermes, P. C. Jennings, P. B. Jensen, J. Kermode, J. R. Kitchin, E. L. Kolsbjerg, J. Kubal, K. Kaasbjerg, S. Lysgaard, J. B. Maronsson, T. Maxson, T. Olsen, L. Pastewka, A. Peterson, C. Rostgaard, J. Schiøtz, O. Schütt, M. Strange, K. S. Thygesen, T. Vegge, L. Vilhelmsen, M. Walter, Z. Zeng, and K. W. Jacobsen, The Atomic Simulation Environment—a Python Library for Working with Atoms, Journal of Physics: Condensed Matter 29, 273002 (2017). doi:10.1088/1361-648X/aa680e.
- [102] E. Runge and E. K. U. Gross, *Density-Functional Theory for Time-Dependent Systems*, Physical Review Letters **52**, 997 (1984). doi:10.1103/PhysRevLett.52.997.
- [103] R. van Leeuwen, Mapping from Densities to Potentials in Time-Dependent Density-Functional Theory, Physical Review Letters **82**, 3863 (1999). doi:10.1103/PhysRevLett.82.3863.
- [104] I. Vasiliev, S. Öğüt, and J. R. Chelikowsky, Ab Initio Excitation Spectra and Collective Electronic Response in Atoms and Clusters, Physical Review Letters 82, 1919 (1999). doi:10.1103/PhysRevLett.82.1919.
- [105] I. Vasiliev, S. Öğüt, and J. R. Chelikowsky, First-Principles Density-Functional Calculations for Optical Spectra of Clusters and Nanocrystals, Physical Review B **65**, 115416 (2002). doi: 10.1103/PhysRevB.65.115416.
- [106] S. L. Adler, Quantum Theory of the Dielectric Constant in Real Solids, Physical Review 126, 413 (1962). doi:10.1103/PhysRev.126.413.
- [107] M. E. Casida, *Time-Dependent Density-Functional Theory for Molecules and Molecular Solids*, Journal of Molecular Structure: THEOCHEM **914**, 3 (2009). doi:10.1016/j.theochem. 2009.08.018.
- [108] J. I. Fuks, L. Lacombe, S. E. B. Nielsen, and N. T. Maitra, *Exploring Non-Adiabatic Approximations to the Exchange–Correlation Functional of TDDFT*, Physical Chemistry Chemical Physics **20**, 26145 (2018). doi:10.1039/C8CP03957G.
- [109] L. Lacombe and N. T. Maitra, Non-Adiabatic Approximations in Time-Dependent Density Func-

- tional Theory: Progress and Prospects, npj Computational Materials 9, 1 (2023). doi:10.1038/s41524-023-01061-0.
- [110] H. Robatjazi, H. Zhao, D. F. Swearer, N. J. Hogan, L. Zhou, A. Alabastri, M. J. McClain, P. Nordlander, and N. J. Halas, *Plasmon-Induced Selective Carbon Dioxide Conversion on Earth-Abundant Aluminum-Cuprous Oxide Antenna-Reactor Nanoparticles*, Nature Communications 8, 27 (2017). doi:10.1038/s41467-017-00055-z.
- [111] L. Zhou, D. F. Swearer, C. Zhang, H. Robatjazi, H. Zhao, L. Henderson, L. Dong, P. Christopher, E. A. Carter, P. Nordlander, and N. J. Halas, *Quantifying Hot Carrier and Thermal Contributions in Plasmonic Photocatalysis*, Science **362**, 69 (2018). doi:10.1126/science.aat6967.
- [112] Y. Kang, S. M. João, R. Lin, K. Liu, L. Zhu, J. Fu, W.-C. M. Cheong, S. Lee, K. Frank, B. Nickel, M. Liu, J. Lischner, and E. Cortés, Effect of Crystal Facets in Plasmonic Catalysis, Nature Communications 15, 3923 (2024). doi:10.1038/s41467-024-47994-y.
- [113] J. S. DuChene, G. Tagliabue, A. J. Welch, X. Li, W.-H. Cheng, and H. A. Atwater, *Optical Excitation of a Nanoparticle Cu/p-NiO Photocathode Improves Reaction Selectivity for CO2 Reduction in Aqueous Electrolytes*, Nano Letters **20**, 2348 (2020). doi:10.1021/acs.nanolett.9b04895.
- [114] J. C. Tully, *Molecular Dynamics with Electronic Transitions*, The Journal of Chemical Physics **93**, 1061 (1990). doi:10.1063/1.459170.
- [115] R. Long and O. V. Prezhdo, *Instantaneous Generation of Charge-Separated State on TiO2 Surface Sensitized with Plasmonic Nanoparticles*, Journal of the American Chemical Society **136**, 4343 (2014). doi:10.1021/ja5001592.
- [116] H. Jin, M. Herran, E. Cortés, and J. Lischner, *Theory of Hot-Carrier Generation in Bimetallic Plasmonic Catalysts*, ACS Photonics **10**, 3629 (2023). doi:10.1021/acsphotonics.3c00715.